Development of new image correction method for the First G-APD Cherenkov Telescope

von

Dominik Wolfschläger

Bachelorarbeit im Fach Physik

vorgelegt der

Fakultät für Mathematik, Informatik und Naturwissenschaften der
RWTH Aachen

im

Juli 2016

angefertigt am

III. Physikalischen Institut A

bei

Prof. Dr. Thomas Bretz

Erstgutachter und Betreuer

Prof. Dr. Thomas Bretz
III. Physikalisches Institut A
RWTH Aachen

Zweitgutachter

Prof. Dr. Thomas Hebbeker
III. Physikalisches Institut A
RWTH Aachen

Eidesstattliche Versicherung

Wolfschläger, Dominik

Name, Vorname

Matrikelnummer (freiwillige Angabe)

Ich versichere hiermit an Eides Statt, dass ich die vorliegende ~~Arbeit~~/Bachelorarbeit/ ~~Masterarbeit*~~ mit dem Titel

Entwicklung eines neuen Bildkorrekturverfahrens für das
First G-APD Cherenkov Telescope

selbständig und ohne unzulässige fremde Hilfe erbracht habe. Ich habe keine anderen als die angegebenen Quellen und Hilfsmittel benutzt. Für den Fall, dass die Arbeit zusätzlich auf einem Datenträger eingereicht wird, erkläre ich, dass die schriftliche und die elektronische Form vollständig übereinstimmen. Die Arbeit hat in gleicher oder ähnlicher Form noch keiner Prüfungsbehörde vorgelegen.

Aachen, 07.07.2016

Ort, Datum

Unterschrift

*Nichtzutreffendes bitte streichen

Belehrung:

§ 156 StGB: Falsche Versicherung an Eides Statt

Wer vor einer zur Abnahme einer Versicherung an Eides Statt zuständigen Behörde eine solche Versicherung falsch abgibt oder unter Berufung auf eine solche Versicherung falsch aussagt, wird mit Freiheitsstrafe bis zu drei Jahren oder mit Geldstrafe bestraft.

§ 161 StGB: Fahrlässiger Falscheid; fahrlässige falsche Versicherung an Eides Statt

(1) Wenn eine der in den §§ 154 bis 156 bezeichneten Handlungen aus Fahrlässigkeit begangen worden ist, so tritt Freiheitsstrafe bis zu einem Jahr oder Geldstrafe ein.

(2) Straflosigkeit tritt ein, wenn der Täter die falsche Angabe rechtzeitig berichtigt. Die Vorschriften des § 158 Abs. 2 und 3 gelten entsprechend.

Die vorstehende Belehrung habe ich zur Kenntnis genommen:

Aachen, 07.07.2016

Ort, Datum

Unterschrift

Abstract

The imaging atmospheric Cherenkov Technique (IACT) compares recorded shower events to Monte Carlo simulated events in order to reconstruct the origin and energy of the shower inducing high-energy gamma ray photon. The image analysis uses simple geometrical parameters to describe an extensive air shower. To be able to get a precise estimate of the properties of the primary particle, a deep knowledge of the imaging properties of the reflector is essential since they have a huge impact on the image quality.

This thesis presents a new image correction method for the First G-APD Cherenkov Telescope (FACT). For this, the images obtained by the actual mirror configuration are compared to those produced by an ideally imaging reflector. The actual photon event is later corrected for the deviation to a perfect image. The method was examined for a pixelised camera layout and tested on shower-like photon distributions proving a maximum improvement of 2% in the image parameters.

Kurzfassung

Die abbildende, atmosphärische Cherenkov-Technik vergleicht aufgezeichnete Schauerereignisse mit Monte-Carlo-simulierten Ereignissen um den Ursprung und die Energie des schauererzeugenden hochenergetischen Gamma-Ray Photons zu rekonstruieren. Zur Bildverarbeitung werden dabei einfache geometrische Parameter verwendet um die ausgedehnten kosmischen Luftschauer zu beschreiben. Um eine präzise Abschätzung von den Eigenschaften des Primärteilchens zu erhalten, ist ein tiefes Verständnis des abbildenden Verhaltens des Reflektors essentiell.

Diese Arbeit präsentiert ein neues Bildkorrekturverfahren für das First G-APD Cherenkov Telescope (FACT). Dazu werden die Abbildungen, welche von der aktuellen Spiegelkonfiguration erhalten werden, mit denen verglichen, die von einem ideal abbildenden Reflektor produziert werden. Das ursprüngliche Photonereignis wird dann um die Abweichung von der perfekten Abbildung korrigiert. Das Verfahren wurde an gepixelten Kamera Layouts untersucht und an schauerähnlichen Photon-Verteilungen getestet, wobei eine maximale Verbesserung von 2% für die Bildparameter gezeigt werden konnte.

Contents

1 Gamma-ray astronomy

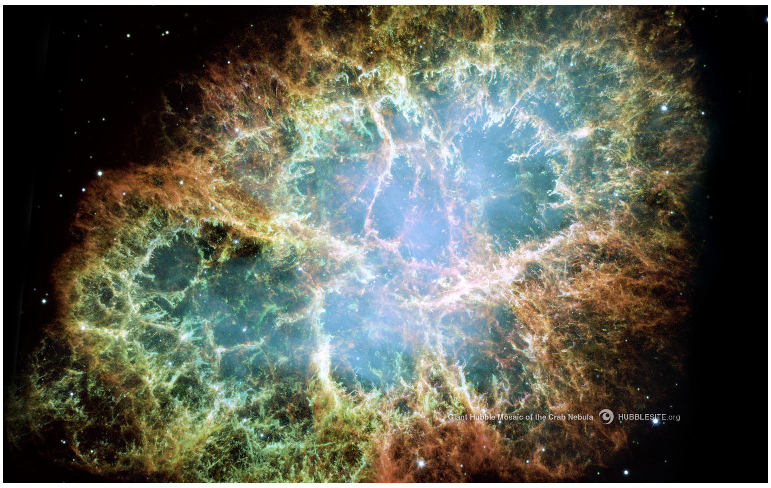

Fig. 1.1.: The crab nebula, the standard candle in gamma astronomy. From [1].

Gamma-ray astronomy is a rather new field in astrophysics and deals with the origins and sources of cosmic ray photons with energies higher than $100\,\mathrm{keV}$. As opposed to charged particles, photons are not deflected by cosmic magnetic fields. As a consequence, they can be used to find, identify and observe the source of their origin and study the underlying acceleration mechanism.

The field has grown strongly within the last 27 years due to the development of the atmospheric Cherenkov technique which led to the detection of the crab nebula in 1989 [2] which can be seen in figure 1.1.

This thesis deals with the FACT telescope which operates in the range of very high-energetic gamma rays (VHEGR) $(0.1 - 100\,\mathrm{TeV})$.

1.1 Cosmic rays

Cosmic rays mainly consist of stable nuclei and particles such as electrons, protons, photons and neutrinos.

The energy spectrum of cosmic ray particles covers several orders of magnitude up to $10^{21}\,\mathrm{eV}$ and can be described by a power law $J(E) \propto E^{\gamma}$, where J is the particle flux per time, area, angle, spatial angle and energy. As shown in figure 1.2 the spectrum can be divided into three parts:

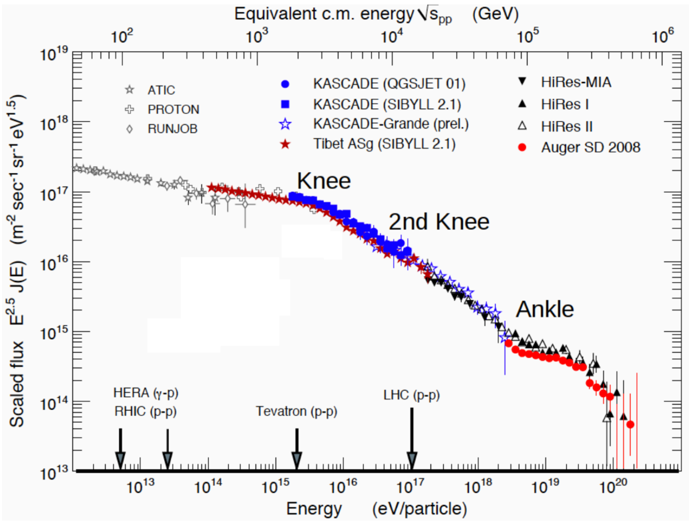

Fig. 1.2.: The figure shows the particle flux per energy over a range of nine orders of magnitude. The accumulated data of the assigned projects is presented. The flux is multiplied by $E^{2.5}$ in order to highlight the characteristic points of the spectrum. From [3]

- $E < 10^{15.4}\,\mathrm{eV}$: The spectrum falls with spectral index of $\gamma = 2.7$ until it reaches the *Knee*. Galactic sources are possible candidates for particles up to this energy.
- $E > 10^{15.4}\,\mathrm{eV}$ and $E < 5 \cdot 10^{19}\,\mathrm{eV}$: The spectrum falls steeper with $\gamma = 3.1$. The galactic magnetic field is not able to keep particles with energies above the knee captured anymore. For energies above the so called *Ankle* extragalactic acceleration mechanisms become favoured.
- $E > 5 \cdot 10^{19}\,\mathrm{eV}$: At the highest energies a sudden further steepening of the spectrum occurs. One possible explanation is the GZK cutoff which prevents high-energetic protons to traverse long distances due to interaction with cosmic microwave background photons [4].

In principle there are two ways to study cosmic rays. Either one builds a detector for space and measures the flux and energy of the primary cosmic rays directly or one builds ground-based detectors. Space-operating detectors are a good choice for the low energy regime of the spectrum. However, the flux of VHE particles decreases very fast, so the small area of space detectors is not able to measure enough VHE particles for reasonable statistics. In order to study VHE radiation, it is possible to build large ground-based telescopes. These are not able to measure the primary cosmic rays directly but they can study the secondaries introduced by these cosmic rays and reconstruct the properties of the primary particle.

1.1.1 Extensive air showers

When primary cosmic rays enter the earth's atmosphere they interact in different ways with it. The particles induce so-called *extensive air showers* (EAS) at approximately $10-20\,\mathrm{km}$ above sea level depending on their energy. For VHE photons the predominant interaction process is pair production which leads to a cascade of electrons, positrons and photons [2].

Heavy, charged particles produce hadronic cascades. Their development is characterised by the production of huge amounts of new particles in each reaction. Moreover, they have a muonic component. In comparison to electromagnetic showers, hadronic showers have a larger scope and a higher number of produced particles.

1.1.2 The Cherenkov effect

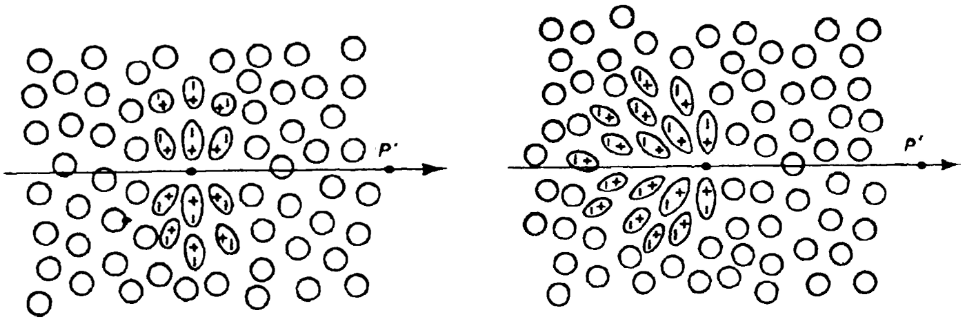

Fig. 1.3.: Illustration of the polarisation of a dielectric medium caused by a charged particle. *Left:* A particle with velocity $v < c_n$. *Right:* A particle with $v > c_n$. The polarisation is situated behind the particle and allows for cherenkov light emission. From [5].

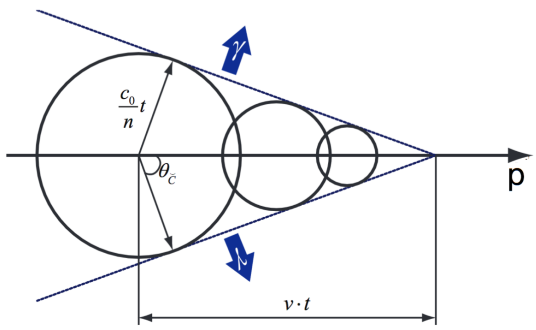

Fig. 1.4.: Huygens construction of the Cherenkov angle. Adapted from [6].

When a charged particle passes through a dielectric medium, it polarises the surrounding atoms. For low velocities, the local dipole field is isotropic, thus it appears to be zero at large distances (cf. fig. 1.3 left). For faster particles this situation changes. When the velocity approaches the speed of light, the dipole field is no longer symmetric in the direction of the particle velocity. The field can be seen at large distances, but the emitted wavelets from each point along the trajectory undergo destructive interference and thus there is no radiation. Only if the velocity v of the particle is greater than the ambient speed of light $c_n = \frac{c_0}{n}$, where n is the refractive index of the medium and c_0 the vacuum speed of light, the polarisation is dragged behind the particle (see fig. 1.3). Now the wavelets of all points along the trajectory of the particle undergo constructive interference at a certain angle, the so-called Cherenkov angle Θ_C. According to Huygens principle, this angle of Cherenkov light emission relative to the direction of the particle is

$$\cos \Theta_C = \frac{c_n}{v}. \tag{1.1}$$

The geometrical construction of this angle is shown in figure 1.4. This angle is approximately 1° in air. Showers induced at a height of $10\,\mathrm{km}$ create a Cherenkov light cone with a radius of max. $120\,\mathrm{m}$ on the ground. The shower can be detected, if the Cherenkov telescope is placed inside the Cherenkov light cone. It is important to point out that every secondary particle with the necessary velocity produces Cherenkov radiation. This means that the primary particle does not necessarily need to have a charge. Moreover, it is not the particle itself that emits radiation, but the atmosphere around the particle.

1.2 Very high-energetic gamma rays

This thesis will be about very high-energetic gamma rays (VHEGR) which will be called *VHE*s within this thesis. Gamma rays are uncharged. Thus, they are not deflected by cosmic magnetic fields and consequently point to the source of their origin. VHEs in particular are gamma rays with an energy of $100\,\mathrm{GeV}$ up to $100\,\mathrm{TeV}$ [7]. However, gamma rays encounter a high probability to interact with other photons of the extragalactic background light when they travel long distances in space . $\gamma + \gamma$-interaction causes electromagnetic cascades in void space reducing the energy of the particle. If this process happens too often, the photons will not have the energy necessary to produce air showers when they enter the earth's atmosphere. This could lead, similar to the GZK cutoff, to a maximum distance for sources of VHE radiation from within our scope [2].

1.2.1 Sources

The sources and mechanisms capable of accelerating particles to very high energies are still unknown and their detection and observation a question of current interest in astrophysics. There are several potential candidates for VHE radiation such as active galaxy nuclei (AGN), blazars [8] and supernova remnants (SNR) like the crab nebula [9]. An overview about the sources and possible acceleration mechanisms is given in [10]. Some of the sources mentioned above show a high flux variability [8, 11] which might be a consequence of the underlying acceleration mechanism. In order to study this, long-term monitoring of these sources is mandatory [12].

2 Imaging Atmospheric Cherenkov Telescopes

This chapter gives a short overview about the principle and idea of an imaging atmospheric Cherenkov telescope (IACT). IACTs use the Cherenkov radiation of extensive air showers to analyse cosmic rays. For this, the telescope takes short video sequences of photon events and compares the image to data fed from Monte Carlo simulations.

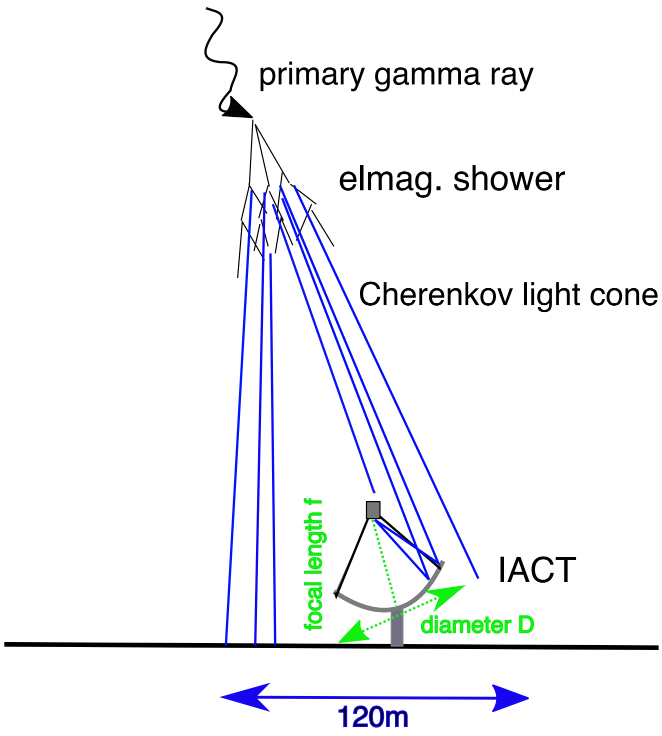

Fig. 2.1.: Principle of an IACT. Primary gammas introduce Cherenkov light emitting electromagnetic showers. The IACT in the Cherenkov light cone collects the Cherenkov radiation and projects it onto a camera equipped with photosensors. Focal length f and diameter D of the reflector are drawn as green dashed lines.

2.1 Principle

IACT are ground-based telescopes which use the whole atmosphere as calorimeter. They are perfectly suited to measure in the VHE regime for two reasons. Firstly, the flux of VHE gamma rays is too small to be measured by satellites and, secondly, the EAS introduced by VHE gamma-rays are not energetic enough to reach sea level [7]. This

implicates, the only remnants of VHE showers are optical Cherenkov photons which arrive at the ground within a few nanoseconds.
If the IACT stands within the Cherenkov light cone of a shower, it collects the Cherenkov photons with its reflector and images them onto a photosensor in the focal plane (see fig. 2.1). The image of the Cherenkov light contains all the information about the shower which further depends on the properties of the shower-inducing particle.
In order to reconstruct these properties, a set of simple geometrical parameters was introduced (see section 2.2) which is able to analyse the cosmic ray particle that induced the EAS.

2.2 Hillas parameters

The image in figure 2.2 represents a geometrical projection of the shower onto a detector plane forming an elliptical shape. The shower image is described by a handful of geometrical parameters, the so-called *Hillas parameters* [14, 13]. These are defined as follows:

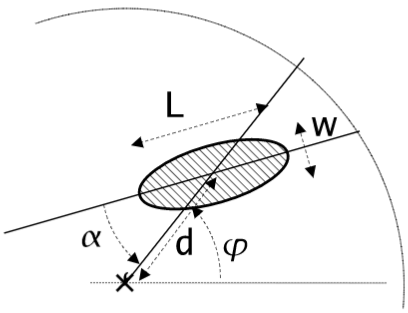

Fig. 2.2.: Geometrical definition of the Hillas parameters. The cross indicates the center of the camera. From [13].

- *SIZE:* The total image amplitude or the number of excess photons.
- *DISTANCE d:* The angular distance from the centre of the camera to the centre of gravity (CoG) of the image. The CoG is the centre of the photon distribution.
- *LENGTH l:* The RMS in the line of sight of the image.
- *WIDTH w:* The RMS perpendicular to the length.
- azimuthal angle of the main axis ϕ.
- orientation angle α.

SIZE and *DISTANCE* are a measure for the energy of the primary particle, whereas *WIDTH* and *LENGTH* can be used to distinguish between different types of showers giving hints for the identity of the primary particle.

2.3 Reconstruction of primary particles

IACTs observing VHE gamma rays are crucial in a reliable differentiation between gamma ray introduced electromagnetic EAS and hadronic showers.
The major difference lies within their shape. Electromagnetic EAS produce more concentrated images in the camera. Therefore, they show a different distribution of the Hillas parameters for different types of showers. In the analysis this can be used as a cut threshold to distinguish gammas from other cosmic ray particles.
To have reliable cuts, Monte Carlo simulation train the analysis algorithms. Comparing the image parameters with those generated by Monte Carlo simulations, it is possible to reconstruct the origin and energy of the shower-inducing primary particle.

The sensitivity of the telescope depends highly on the quality of the Monte Carlo simulations which in turn requires a deep understanding of the imaging process and the properties of the telescopes. To find suitable cut thresholds, a good image resolution is mandatory. This thesis picks up this point correcting the images for optical aberrations.

3 FACT - The first G-APD Cherenkov telescope

FACT is a ground-based gamma ray telescope using the Imaging Atmospheric Cherenkov Technique. It is located $2200\,\mathrm{m}$ above sea level at Roque de los Muchachos, La Palma, and has been operating since October 2011. The telescope can be seen on the photograph in figure 3.1. FACT is the first telescope of the **DWARF** (Dedicated Multiwavelength AGN Research Facility) project which aims to install more telescopes like FACT around the world to enable long-term monitoring of VHE sources. Consequently, the telescope is designed to have an enlarged duty cycle using solid state based photosensors as a special technical feature. An overview about the specifications of FACT is given in table 3.1.

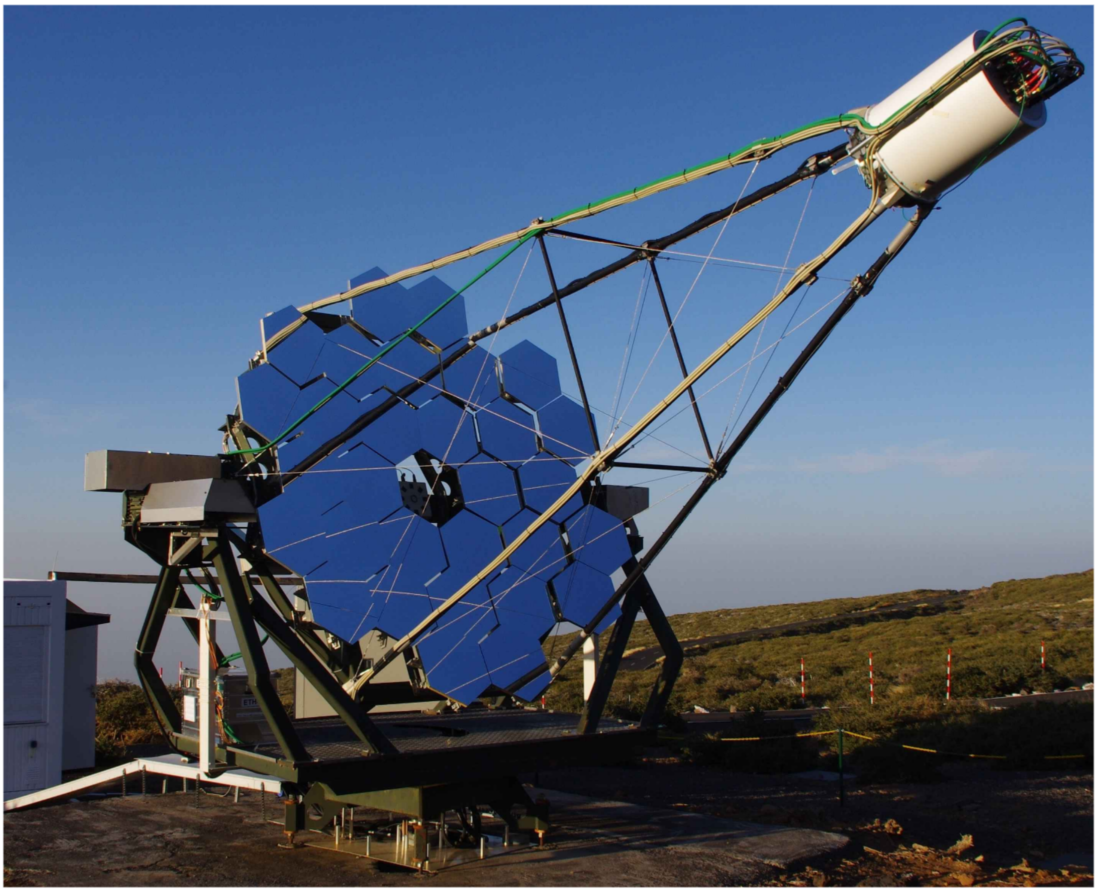

Fig. 3.1.: The First G-APD Cherenkov Telescope at Observatorio Roque de los Muchachos. Photograph taken from [15].

3.1 Solid state photomultipliers

One major goal of the FACT project is to prove the suitability of silicon photomultipliers (SiPM) for gamma ray observations. FACT is the first Cherenkov telescope using these Geiger-mode avalanche photodiodes (G-APD) instead of common photomultiplier tubes (PMT) in order to measure the Cherenkov light of VHE induced air showers.

3.1.1 Basic functioning

G-APDs are solid state photosensors which are operated above their break-down voltage in the so-called Geiger-Mode. Thus, an incident photon produces an electron-hole pair in the depletion zone which is accelerated by the electric field originating from the bias voltage. Consequently, the electron-hole pair is able to produce more pairs that initialises an avalanche leading to a complete discharge of the photo diode. The released charge is a unique property of each diode and depends on the difference between the bias voltage and the breakdown voltage. The latter is strongly temperature dependent. As a consequence, a real time feedback system was implemented by the FACT community to compensate for the effects of light level and temperature. [16].
The major advantage of SiPMs in comparison to PMTs in gamma ray applications is that they can be operated even under harsh conditions like full moon without showing any ageing. Moreover, they have a photon detection efficiency (PDE) of $\sim 50\%$ which exceeds that of common PMTs. This number states how many of the incident photons are finally detected.

3.1.2 Camera/ Light concentrators

The camera consists of 1440 pixels each suited with a $3 \times 3\,\mathrm{mm}$ photosensor with 3600 G-APDs. In order to minimise the insensitive area due to the dead space between the photosensors, light concentrators are glued on top of each. Following the description in [17], cones with tilted parabolic shapes - so-called Winston-Cones - show a maximum concentration ratio and only small smearing for light transmission near the cutoff angle Θ which is determined by the F-number of the telescope. Consequently, the light cones help to reduce stray background light, because only light which was reflected by the mirrors can enter the light cones and reach the detector [18].
For FACT solid light concentrators with a hexagonal entrance aperture with a diameter of $9.5\,\mathrm{mm}$ and a quadratic exit aperture of $2.8\,\mathrm{mm}$ were designed (see fig. 3.2).

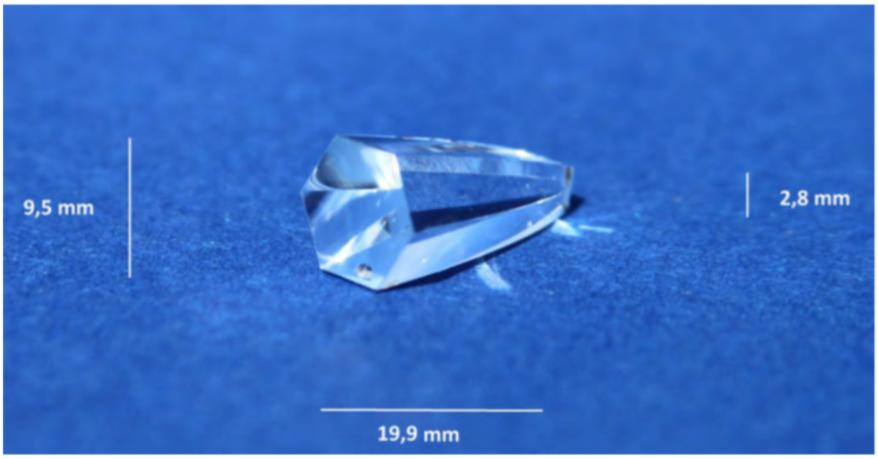

Fig. 3.2.: Photograph of a light cone used for the FACT camera. From [19].

3.2 Reflector design

The reflector consists of 30 spherical, aluminium coated mirrors currently arranged in a configuration which is half parabolic and half Davies Cotton [15, 20]. The mirrors are hexagonal. The Field of View (FoV), which is twice the angle the reflector spans looking from the centre of the camera (see fig. 4.3 on page 17). The values given in table 3.1 lead to a FoV of $4.5°$ for FACT. Originally, the reflector was arranged in total Davies Cotton design [19] because of the superior focusing properties of this arrangement [21]. In Davies Cotton design, all mirrors have the same focal length and are arranged on a spherical surface with the radius of their focal length. Their images are such superimposed at the target that the point spread function (PSF) is minimal.
The Davies Cotton design has an advantage in spatial resolution but has a inferior temporal resolution compared to mirrors aligned on a parabolic surface. In May 2014 the reflector was realigned in order to improve the temporal imaging quality [20]. Therefore the arrangement of the reflector was altered from pure Davies Cotton geometry to a Hybrid geometry approximately half Davies Cotton half parabolic. The new reflector design was realised using a new alignment technique called "bokeh" [22]. The fine alignment was carried out with the "NAMOD" system [23]. Now, the reflector can be described by the expression

$$G_{\mathrm{Hy}}(\alpha) = \alpha G_{\mathrm{DC}} + (1-\alpha) G_{\mathrm{PA}} \tag{3.1}$$

with $\alpha = 0.52$ and G_{DC} a parameter describing the Davies Cotton geometry, G_{PA} a parameter describing the parabolic geometry and G_{HY} a parameter describing the compound geometry [20]. It is possible to adjust the hybrid parameter α in order to obtain a different mirror configuration.

Tab. 3.1.: General information and components of FACT. Adapted from [20].

number of mirrors	30
focal length f	488.9 cm
effective diameter of aperture D_{eff}	326.1 cm
maximal diameter of aperture D_{max}	392.6 cm
effective F-number, f/D_{eff}	1.5
minimal F-number, f/D_{max}	1.25
Field of View (FoV)	$4.5°$
diameter of image sensor	39 cm
number of pixels	1440
energy sensitivity	100 GeV - 10 TeV

4 Ray tracing simulations

This thesis uses ray tracing to simulate the reflection of Cherenkov photons at the mirrors of the telescope. The image for the analysis is taken in the focal plane of the reflector. A suited ray tracing program is provided by FACT through the ROOT-based [24] standard analysis software **MARS**. This chapter explains how to perform ray tracing with MARS and examines the imaging properties of the reflector in order to prove the symmetry of the FACT reflector.

4.1 MARS CheObs ed.

MARS CheObs ed. (**M**odular **A**nalysis and **R**econstruction **S**oftware - **Che**renkov **Obs**ervation **ed**ition) is the Cherenkov telescope event-based extension of the analysis package **MARS** [25, 26].
The package consists of several modules which perform different tasks [27].

- CALLISTO (**CAL**ibrate **LI**ght **S**ignals and **T**ime **O**ffsets)
  Purpose: Calibrating the raw data.

- STAR (**St**andard **A**nalysis and **R**econstruction)
  Purpose: Image cleaning and determination of image parameters.

- GANYMED (**G**ammas **A**re **N**ow **Y**our **M**ost **E**xciting **D**iscovery)
  Purpose: distinguishing gamma events from background.

- SPONDE (**Sp**ectrum **On** **DE**mand)
  Purpose: Calculating the energy of the shower-inducing primary particle by comparison with Monte Carlo data.

- CERES (**C**amera **E**lectronics and **Re**flector **S**imulation)
  Purpose: Performing the ray tracing and simulating the camera.

The modular setup allows for fast and easy adaption of parts of the software for other telescopes because the modules for analysis and telescope setup are completely independent from each other [28]. In this thesis, only a part of the module **CERES** will be utilised.

4.1.1 CERES

CERES performs the reflection and simulates the camera. Thus, it is responsible for the ray tracing. The algorithms need to be fed with the information about the reflector setup, the camera components etc.. This data is stored in so-called "resource files" - simple text files containing the data of the position and orientation of each individual mirror and their focal length. The resource file **fact_reflector_since_alignment_in_May_2014.txt** contains the current reflector setup since the last realignment in 2014 (see appendix chapter A) [20].

4.1.2 Reflector geometry

In addition to the actual mirror configuration, other resource files with modified reflector setups were created following the formulae in chapter three in [20] and using the information about the mirror position from figure 4.1 from [19]. The most important resource file is the one containing the setup for an ideal Davies Cotton reflector. In contrast to the actual reflector, the ideal setup is arranged in a perfectly symmetrical way around the centre of the reflector. No restriction from the telescope mount were taken into account.
The setup is stored in **ideal_davies_Cotton.txt** and can be found in the appendix in chapter A. The importance of this resource file is that the ray tracing results can be used to compare the spatial imaging quality of the actual configuration to the enhanced (Davies Cotton) arrangement.

4.1.3 A perfect mirror

The challenge lies within the geometry of the FACT reflector and the camera. The reflector has a curved surface which means that a parallel incident wavefront will obtain a curved profile after being reflected. This curved wavefront is further imaged on a plane camera and thus lacks from field curvature. Field curvature is an optical aberration, indicating that it is not possible to focus the image equally on all points of the camera. Moreover, rays reflected at great distances from the symmetry axis are focused at a different point along the telescopes symmetry axis than rays from the centre of the reflector. This is known as spherical aberration [29, 30].
All together, these aberrations cause a shift in the position leading to an image which lies further away than the perfect image. The idea is now to compare the position of the centre of gravity of a photon event to the expected position for a perfect mirror. The

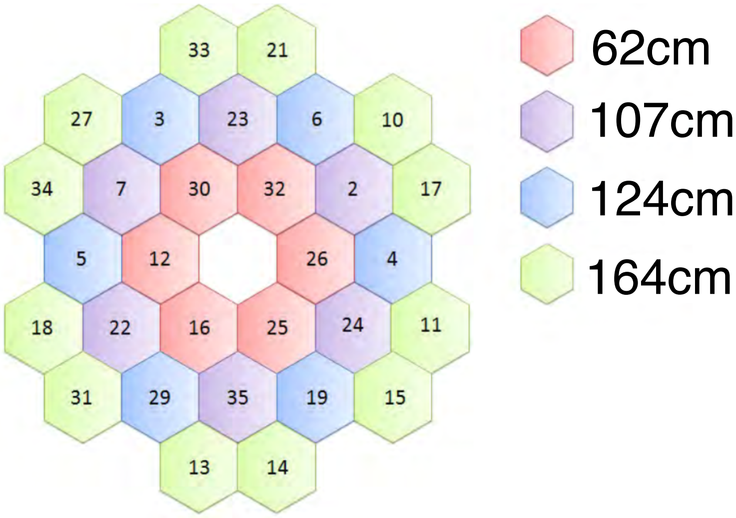

Fig. 4.1.: Reflector layout for a segmented reflector using hexagonal mirrors. The number is the identification number which can be found on the back side of the actual mirrors. All mirrors are positioned at one of the four given radii. The colour labels the distance of the centre of the mirror to the centre of the reflector. Adapted from [19].

only mirror complying this prerequisite is a plane mirror. The expected position can be found observing a ray - the so-called *principal ray* - which is reflected at the centre of the telescopes reflector according to the law angle of incidence equals angle of reflection.

4.2 Ray tracing simulation

Given a resource file and additional information about the light source, the position of the telescope and its pointing position, CERES performs the ray tracing. It stores the data from each photon in the current ray tracing plane. For debugging purposes the current status of the data is filled into five histograms which contain the position, the direction, the time profile, the wavelength-distribution and the production height in the corresponding mirror plane. These histograms are further displayed in a canvas (see fig. 4.2). The investigations in this thesis neglect parameters such as wavelength and production height. The latter is infinity for a point like source. Therefore, the two histograms do not contain necessary information.
The first tab displays the photons how they are generated by the light source. The second tab shows all the photons that can potentially hit the reflector whereas the third displays the photons that actually hit the mirror. The fourth maps the photons when they reach the camera plane and the fifth tab shows the photons in the camera plane that crossed the camera plane within the area of the camera. All data is stored in a .root-file. In principal MARS allows this for other data types too, but for further analysis ROOT-Trees are suited best (for more information see the MARS source code). For the

FACT geometry ray tracing was performed for all tilt angles from 0-3° in 0.05° steps and every rotation angle around the reflector's symmetry axis from 0-359° in 1° steps.

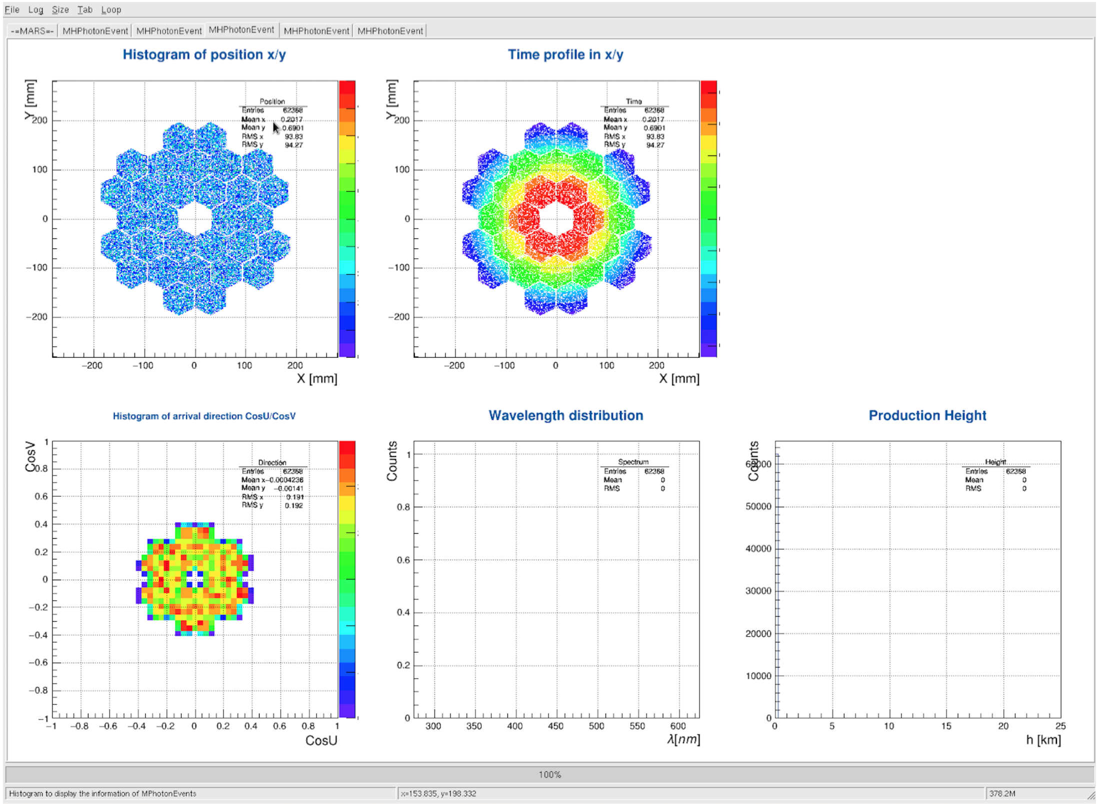

Fig. 4.2.: Output canvas for the ray-tracing with MARS. The current tab shows the photon data at the reflector. There is no mirror in the centre of the reflector because it would be shielded from light by the camera housing. From [19].

Tab. 4.1.: Settings of the ray tracing simulations for the FACT reflector

resource file	fact_reflector_since_alignment_in_May_2014.txt / ideal_davies_cotton.txt
light source	point-like ⇒ parallel light
production height	∞
number of photons	100000
tilt angle Θ_{tilt}	0.2°, 0.7°, 1.2°, 1.7°, 2.2°
azimuth angle Φ	0 – 359°

4.3 Ray tracing results

The first aim of this thesis is to find a function that describes the difference between the reflection at the curved mirror and the reflection at a mirror without any aberrational effects - a plane mirror.

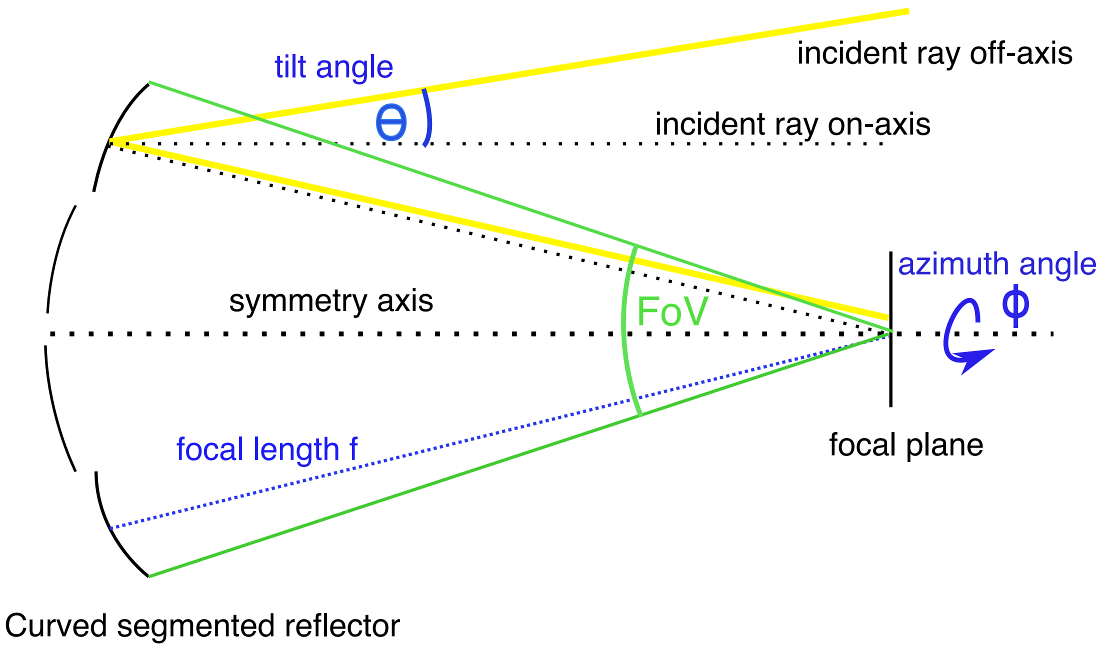

Fig. 4.3.: Illustration of the symmetry axis and the definitions for a segmented mirror telescope like an IACT.

4.3.1 Symmetry of the FACT mirror

In order to find the radial dependency, the difference

$$CoG_{\text{actual}} - CoG_{\text{expected}} \tag{4.1}$$

is calculated for each tilt angle respectively. CoG is the abbreviation for *centre of gravity* and is the mean position of the photon distribution (compare the definition of the Hillas parameters in section 2.2). Thereby, CoG_{actual} is the CoG produced by the actual mirror configuration and CoG_{expected} is the position of the principal ray. Before determining the radial dependency, it must be shown that the imaging properties are independent for rotations around the symmetry axis of the reflector. For this purpose, the deviation in radial and tangential (azimuthal) direction and the total deviation from the expected CoG of a point source are observed for each azimuth angle. All this is executed for five tilt angles: $0.2°$, $0.7°$, $1.2°$, $1.7°$ and $2.2°$. An overview about the quantities and definitions used here is given in figure 4.3. The position of the CoG for all possible angular combinations is displayed in figure 4.4 in the reference frame of the camera centre. There is no major visible difference between the different reflector settings in these plots. Therefore, it is necessary to examine the deviations from the expected position in each direction in more detail.

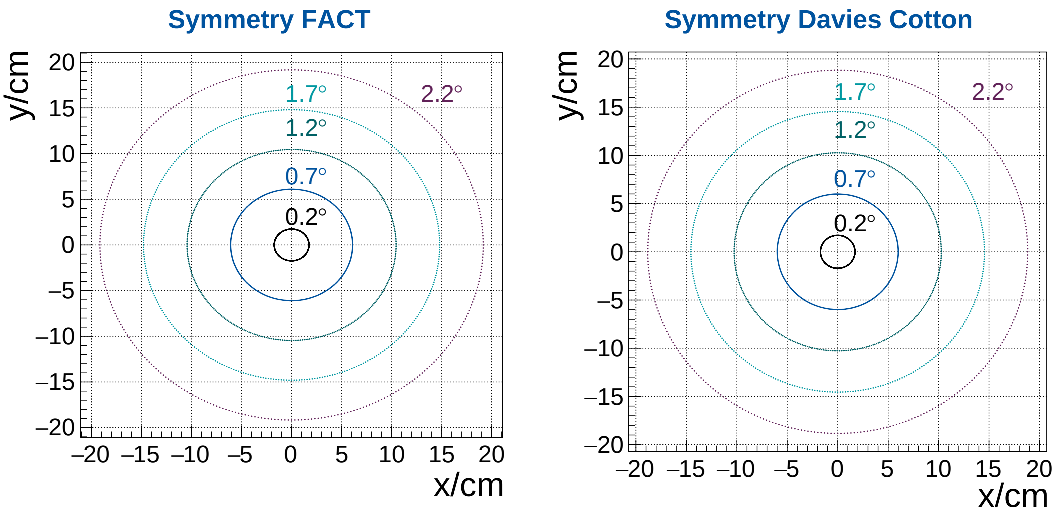

Fig. 4.4.: Positions of the CoG for each direction of the light of a point source. For both setups no major deviations are noted. The circles correspond to the tilt angles included in the corresponding colour. This colour code will be used for the further investigations as well.

Radial deviation

The extension of an object imaged by a rotationally symmetric optical system is usually given by the *apparent size* or by the vertical and horizontal angle of vision. This means that the angular deviation from the centre of camera is observed from the centre of the reflector at distance $f = 488.9\,\mathrm{cm}$. First, the CoG is transformed into polar coordinates $(x, y) \to (r, \phi)$ in the camera plane. In order to get the angular distance in degrees,

$$\Theta_{\mathrm{CoG}} = \arctan\left(r_{\mathrm{CoG}}/f\right) \approx r_{\mathrm{CoG}}/f \tag{4.2}$$

needs to be evaluated. Having a FoV of $4.5°$, the small-angle approximation is a legitimate simplification. From now on, the CoG refers to the quantity given in units of degree.
The radial deviation is further the vertical angle of vision

$$\Delta\Theta = \Theta_{\mathrm{CoG}} - \Theta_{\mathrm{tilt}}. \tag{4.3}$$

In figure 4.5 it is possible to see, why it is necessary to correct the image for aberrational effects. The deviation from the expected radial position is one order of magnitude larger than for an ideal Davies Cotton mirror.

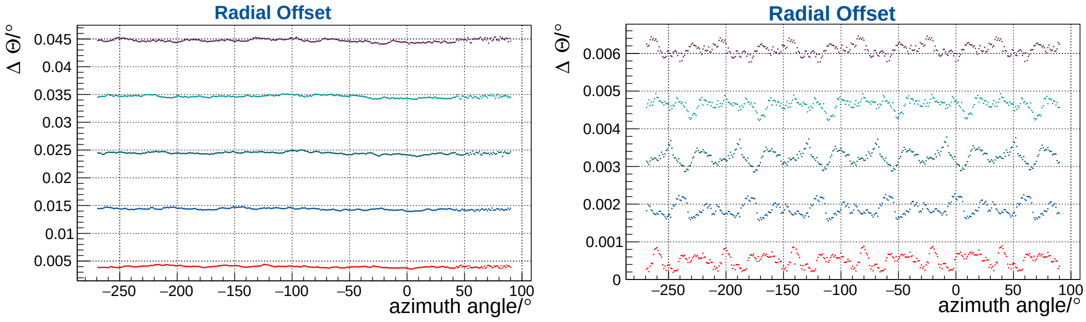

Fig. 4.5.: Radial deviation ΔΘ for FACT reflector (*left*) and Davies-Cotton arrangement (*right*). Colours refer to the tilt angles in fig. 4.4.

The explanation for the oscillations in the radial offsets for the Davies-Cotton design, lies within the geometry of the reflector. The diameter of the total reflector changes depending on the azimuthal angle of incidence of incoming light. This is due to the hexagonal shape of the individual mirrors which does not from an radially isotropic reflector (compare fig. 4.6). For larger diameters the effect of optical aberrations increases which leads to a shifted position of the photon distribution.

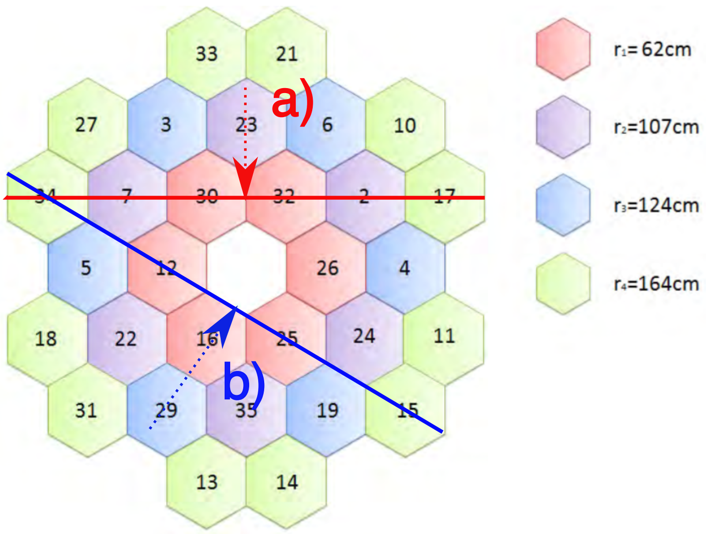

Fig. 4.6.: Explanation of the oscillations in fig. 4.5. Light with incident direction *a)* sees a smaller maximal diameter than light with incident direction *b)*. Consequently, optical aberrations contribute more strongly for b) .

Azimuthal deviation

The azimuthal deviation is equivalent to the horizontal angle of vision. Knowing the azimuthal direction Φ of the incident light rays, the azimuthal deviation in the frame of the camera plane is

$$\Delta\phi_{\text{camera}} = \phi_{\text{CoG}} - \phi. \tag{4.4}$$

Based on this angle and r_{CoG}, the radian measure b for the offset can be calculated:

$$\sin \frac{\phi_{\mathrm{camera}}}{2} = \frac{b}{2 r_{\mathrm{CoG}}}. \tag{4.5}$$

Moreover, the object distance g can be obtained by

$$g = \sqrt{f^2 + r^2}. \tag{4.6}$$

In the next step, the horizontal angle of vision can be calculated approximating the radian measure by a straight line. This assumption is justified due to the narrow FoV of FACT. The telescope only observes sources up to an angle of $2.25°$. This means that the small-angle approximation is a suited simplification. It therefore follows that

$$\tan \frac{\epsilon_\phi}{2} = \frac{b}{2g} = \frac{r \sin\left(\phi_{\mathrm{camera}}/2\right)}{\sqrt{f^2+r^2}} \tag{4.7}$$

$$\Rightarrow \epsilon_\phi \approx \frac{\phi_{\mathrm{camera}}}{\sqrt{1+f^2/r^2}}. \tag{4.8}$$

ϵ_ϕ is the deviation from the expected position in azimuthal direction. Consequently, it will be called $\Delta\phi = \Delta\phi_{\mathrm{camera}}$ from now on.

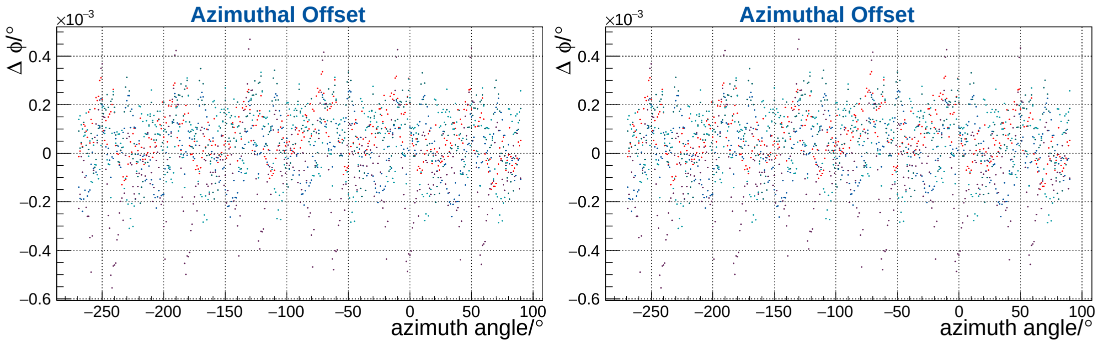

Fig. 4.7.: Azimuthal deviation $\Delta\phi$ for FACT reflector (*left*) and Davies-Cotton arrangement (*right*).

As shown in figure 4.7, the azimuthal deviation lies one order of magnitude below the radial offset for the FACT reflector. For the DC configuration it is normally distributed around zero (see the histograms in the appendix in figure A.1). This implicates that the origin of the azimuthal deviation is due to statistical effects and does not show any systematics.

Total deviation

Using the small-angle approximation, the total deviation is calculated using the Pythagorean theorem

$$\Delta = \sqrt{\Delta\phi^2 + \Delta\Theta^2}. \tag{4.9}$$

This means that we can neglect the azimuthal deviation for our further analysis for the FACT reflector, because the radial offset is one order of magnitude larger and thus dominates the total deviation. Even for the Davies Cotton arrangement, it makes no difference because it statistically fluctuates around zero (cf. fig. 4.5 and 4.8, right figure respectively).

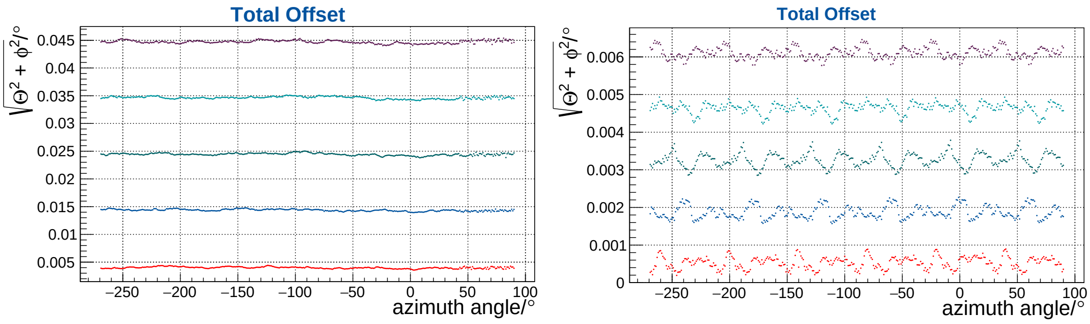

Fig. 4.8.: Total Offset $\Delta\Theta$ for FACT reflector (*left*) and Davies-Cotton arrangment (*right*).

Comparing both graphs in figure 4.8 one can see that the total deviation is more or less constant for FACT. Nevertheless, there appears to be a dent between $-50°$ and $+50°$ which has an amplitude of $\approx 0.001°$. This is a relative change in the position of roundabout 2%. The oscillation observed at the Davies Cotton reflector causes a shift of roughly 6%.

Moreover, the dent only appears at one position while a permanent oscillation can be observed for the Davies Cotton arrangement. This means that no systematic azimuthal dependency can be found for FACT and the reflector can be considered to be adequately symmetric. We will further calculate the mean over all azimuthal angles and take the sample standard deviation instead of the standard error of the CoG as uncertainty in order to account for the dent.

This is statistically equivalent to estimating the deviation from the expected position when only the tilt angle is known but not the azimuthal angle. The uncertainty for the CoG is subsequently affected by not knowing whether it lies in the range of the dent or not.

4.3.2 Radial deflection for the FACT reflector

Ray tracing simulations were performed for 61 tilt angles from $0-3°$ in $0.05°$ steps and for 360 azimuthal angles from $0-359°$. The CoG was thereby determined for each configuration based on the settings from table 4.1.

According to the investigations in the previous section, the mean and RMS over all azimuthal positions is calculated. The averaged CoG is subtracted by the expected CoG and plotted versus the expected CoG (see fig. 4.9).

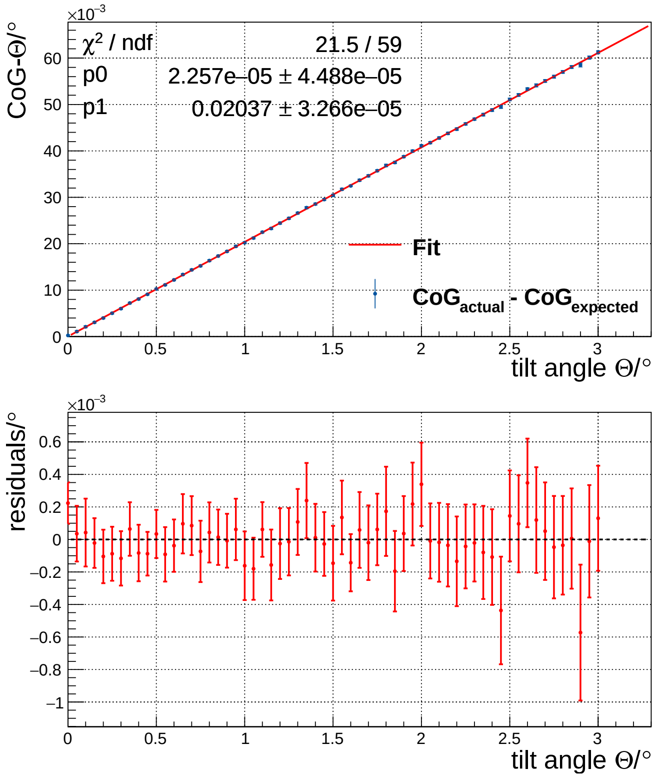

Fig. 4.9.: Radial dependency of the CoG for parallel light. Each point in the upper figure represents the mean over 360 azimuthal angles. The uncertainty was estimated using the spread of the sample. The lower figure shows the residuals for the linear fit.

Figure 4.9 shows a linear relationship between the deviation of the actual position and the expected position. The actual CoG is shifted by a factor

$$\eta = \frac{0.02^\circ}{1^\circ}. \tag{4.10}$$

The offset can be neglected because it passes the origin within its uncertainty.
As a consequence, the law describing the actual angular distance r_{act} from the centre of the camera to the expected position r_{exp} is

$$r_{\text{act}} - r_{\text{exp}} = \eta r_{\text{exp}} \tag{4.11}$$

$$\Leftrightarrow r_{\text{exp}} = \frac{r_{\text{act}}}{1.02}. \tag{4.12}$$

Knowing this relationship, it is possible to subsequently correct the photon position by this factor.

5 An image correction method for FACT

In this chapter a new image correction method to compensate for optical aberration will be introduced. This correction is not about any special aberration in particular but deals with the whole bunch of aberrations at once.

5.1 Principle of the image correction method

Knowing the radial dependency from chapter 4, it is theoretically possible to record the position of each photon in the camera plane and then correct each individual photon in radial direction towards the centre of the camera accordingly. The result is a corrected image with the CoG positioned at the same position as an image obtained by a perfect mirror.

However, the resolution of the camera is not infinitely precise, FACT can only read the output of the 1440 SiPMs and subtract the noise phenomena such as dark counts and crosstalk (for more information see [16]) to get to know the number of photons in each bin. This is equivalent to filling photons into a two-dimensional histogram with hexagonal bins.

The idea is now to shift the centre of each bin radially towards the centre of the camera and afterwards perform the image analysis. In order to calculate the CoG and the RMS in both radial and tangential direction, the binning is accounted for by weighting the centre of each bin with its content. It follows

$$\overline{r} = \sum_{i=0}^{M} \frac{r_i \cdot n_i}{N} \tag{5.1}$$

$$r_{\mathrm{RMS}} = \sqrt{\sum_{i=0}^{M} \frac{(r_i - \overline{r})^2 \cdot n_i}{N-1}} \tag{5.2}$$

where M is the number of bins, $\sum n_i = N$ whereby n_i is the number of photons and r_i the radial distance of the i-th bin.

Each hexagonal bin of FACT covers approximately 0.11° of the FoV of the telescope. To keep the demonstration of the image correction method as simple as possible, the binning will be performed using square bins with a side length of 0.11° (see fig. 5.1).

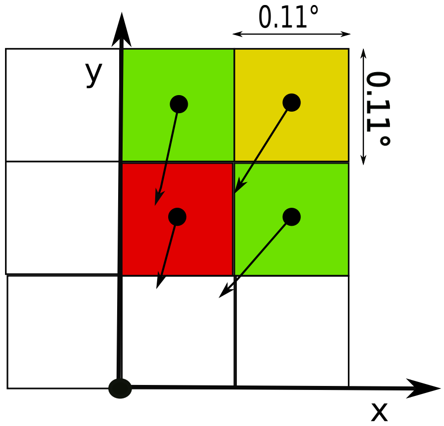

Fig. 5.1.: Binning and correction for the image analysis. The camera plane is divided into a grid of squares with a side length of $0.11°$. The centre of the bins are shifted towards the centre of the camera. The colour indicates the weight of each pixel.

5.2 Performance of the image correction

The image correction is now applied on images in the focal plane of the camera. In order to study the influence of the bins, the tilt angle was increased in steps of $0.01°$ which is significantly smaller than the bin width (see tab. 5.1). The CoG and the RMS in both directions were calculated before and after the application of the image correction unbinned and binned respectively. As a consequence of the binning, it would actually be necessary to take an uniform error $d/\sqrt{12}$ into account, where d is the width of a pixels. This error is due to the camera layout and thus cannot be reduced. This error will be disregarded for the evaluation and fits in this thesis because this thesis shall demonstrate that the presented method is in principle able to contribute to an improvement of the sensitivity of FACT.
Moreover, there are statistical errors due to the fluctuations in the produced photon positions. However, using ray tracing simulations it is always possible to produce enough statistics to make this statistical error small in comparison to the result. Because of this, at least 100000 photons were produced for each ray tracing process. As a consequence, the χ^2 and uncertainty of any fit parameter in the following chapters do not have any informative value. Nevertheless the obtained fit parameters can be used to examine the impact of the image correction method. Of course, a full statistical investigation of the method will be needed, but for this, Monte Carlo simulated shower events are mandatory to study the impact on the distributions of the image parameters. All this is beyond the scope of the thesis and would be subject of a whole thesis again.
Choosing the azimuthal angle to be $0°$ causes the image to be located along the y-axis of the camera and to always be split up into two pixels in x-direction. This situation shows the maximum effect of the binning in y-direction and no effect in x-direction. Thus, only the radial RMS needs to be examined. Any other possible azimuth angle shows the same phenomena split up into both directions and both RMSs.

Tab. 5.1.: Settings of the ray-tracing simulations to examine the binning.

resource file	fact_reflector_since_alignment_in_May_2014.txt
light source	point-like ⇒ parallel light
production height	∞
number of photons	100000
tilt angle Θ_{tilt}	$[0.05 - 2.7]$ in $0.01°$ steps
azimuth angle Φ	$0°$

5.2.1 Binning and correction of the centre of gravity

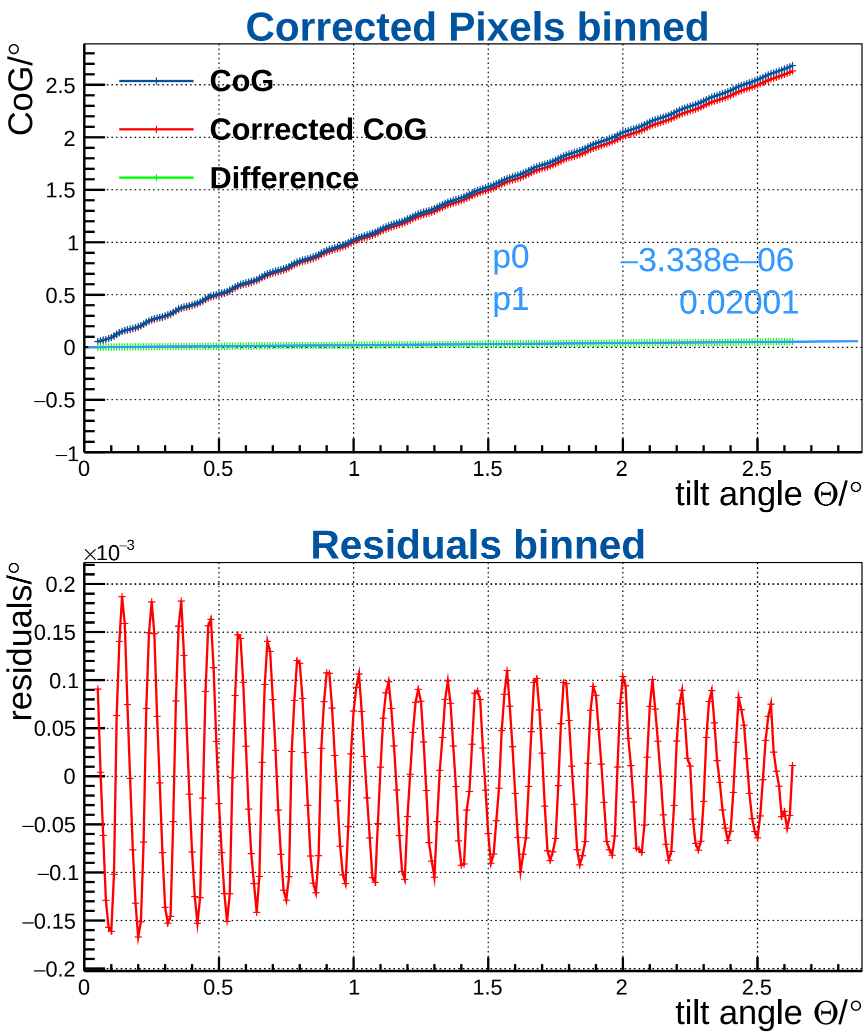

Fig. 5.2.: *Upper figure*: Image correction for binned data. The binning causes a slightly stepwise shape which can be seen especially for low tilt angles. *Lower figure* Residuals of the difference of the data. A pronounced oscillation can be observed.

The centre of gravity before and after the image correction is plotted versus the tilt angle Θ for both binned (fig. 5.2) and unbinned (fig. 5.3) sets of data. It is possible to see that the binning causes a stepwise curve shape for both corrected and original

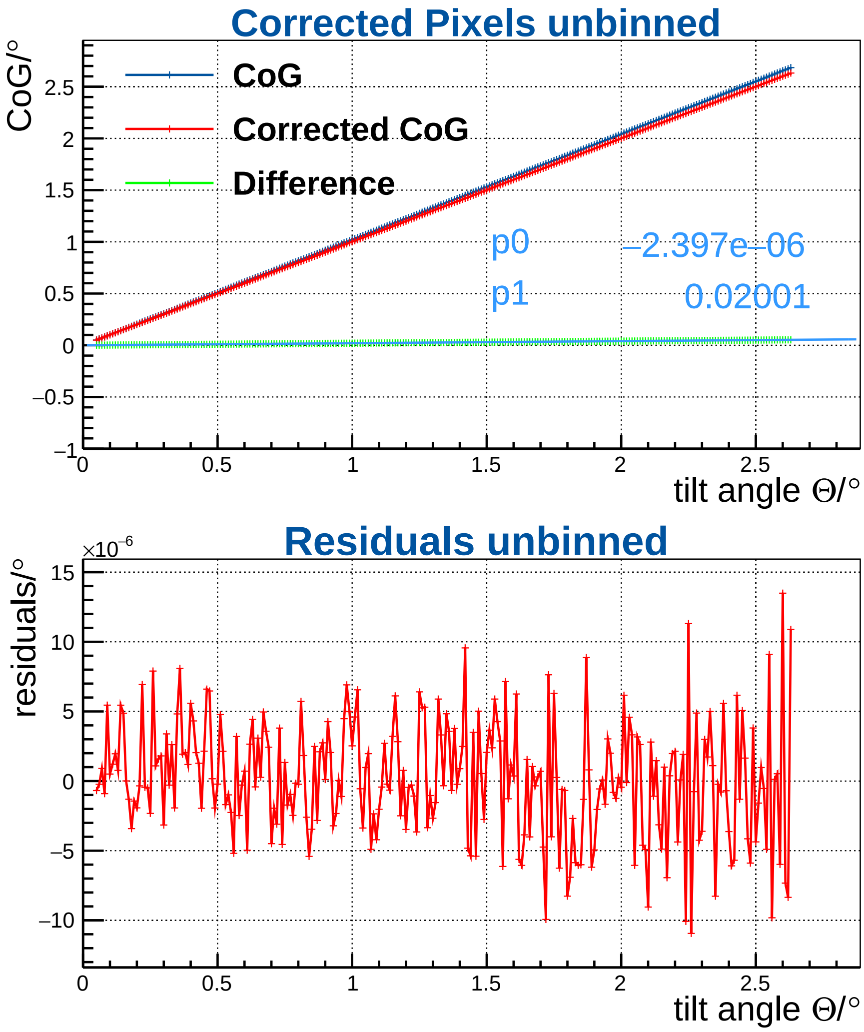

Fig. 5.3.: *Upper figure*: Image correction for the unbinned data. *Lower figure*: Residuals of the unbinned data.

data as opposed to the unbinned data. Fitting a balance line to the difference of both curves (turquoise line in upper fig. in 5.2) shows the applied correction factor of 2%. Observing the residuals of the binned data, an oscillation can be discovered in contrast to the unbinned case (fig. 5.3 bottom). Thereby, the number of minimums or maximums corresponds to the number of pixels along the y-axis in the camera plane. The oscillation occurs because there are only a discrete number of positions where the correction factor can be applied to. These positions are weighted with the number of photons in the corresponding bin. Assuming a distribution that lies in one pixel only, an application of the image correction would shift the mean exactly by $\eta = 0.02°/1°$. When some photons move to the next outer/inner bin, the correction applies stronger/weaker at this second bin due to the linear character of the correction method. The corrected CoG is therefore further away/nearer situated than for the unbinned case. For large tilt angles, the projection of the distribution splits up onto several pixels which causes the dampening seen in the residuals for the binned data.

5.2.2 Binning and correction of the RMS

The plots in figure 5.4 and 5.5 show the development of the radial RMS and the difference for the original and corrected data. To reveal how the RMS changes due to the binning, a third order polynomial was fitted to the unbinned data. This polynomial was chosen because lower orders did not describe the shape properly. It appears the unbinned data is a lower boundary for the binned case. This occurence mainly depends on the distribution of the photons because assuming again a distribution that lies in exactly one bin, equation (5.2) for the RMS yields 0. This case begins to act especially for the low tilt angles for the case observed here. If the RMS of the unbinned distribution is small in comparison to the bin width but spans several bins which is the case for the image of a point source for FACT, the unbinned data forms a lower boundary.

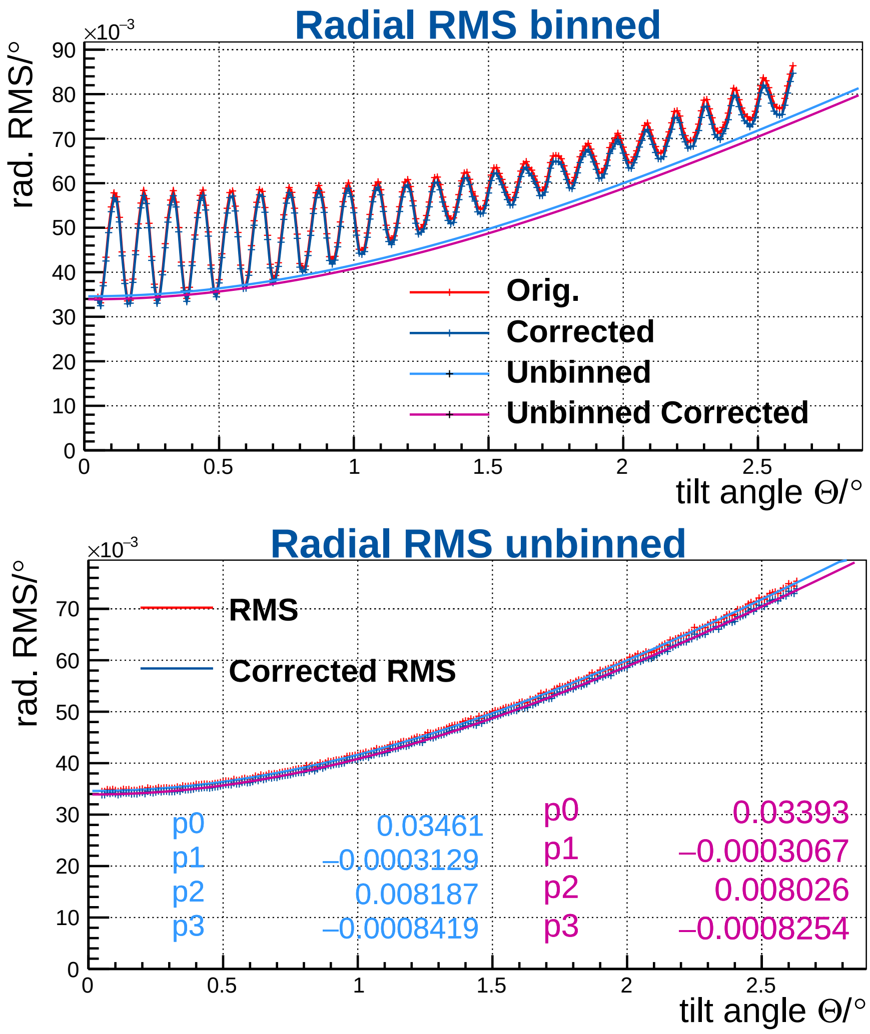

Fig. 5.4.: *Upper figure*: Development of the radial RMS for binned data. The fits from the unbinned data were drawn into the upper figure to show that they form somehow a lower boundary for the RMS of the point-like source. The same oscillation as for the CoG can be observed. *Lower figure*: Unbinned RMS for comparison only.

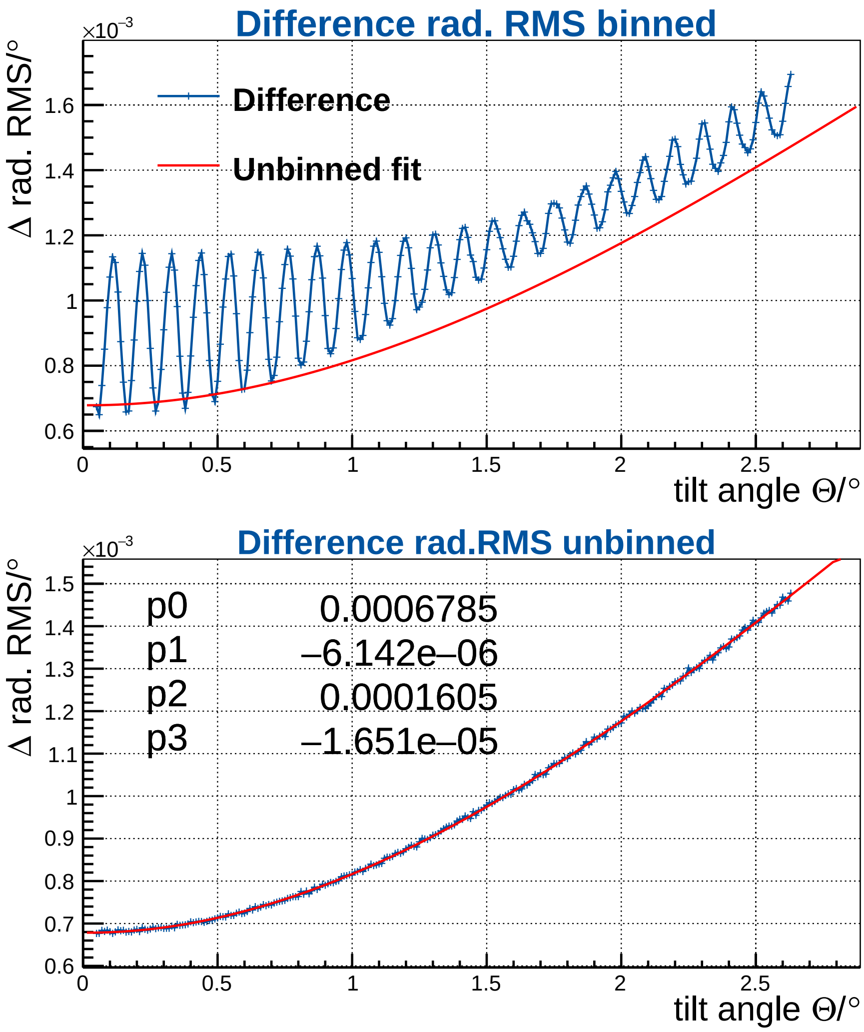

Fig. 5.5.: *Upper figure*: Difference of the binned RMS and fit of the unbinned difference of the unbinned RMS for comparison. An oscillation similar to the CoG can be observed. Moreover, the unbinned difference seems to be a lower boundary again. *Lower figure*: Difference of unbinned data for comparison only.

Again, there is an oscillating behaviour in the difference of the original and corrected RMS (cf. fig. 5.5). The reason is similar to the CoG. If the binned RMS is large, the occupied bin centres use to be further away from the mean position and such the image correction has more impact.

All in all, the binning causes an mostly overestimated RMS for small photon distribution like the one produced by the point source here. Therefore, the image correction methods needs to be tested with showers of typical size in the operational mode for FACT.

5.3 Application on shower events

In application the correction method needs to be performed on real shower data. In operation, MARS calculates the the Hillas parameters which will be done here too accordingly. Shower events, induced by primary particles with an energy in the operating range of FACT, have a two-dimensional gaussian profile and usually a *WIDTH* of $0.15 - 0.25°$ and a *LENGTH* of $0.3 - 0.5°$ in the focal plane. In order to show the maximal effect, only two extreme shower distributions will be examined. They are implemented such that they produce a gaussian profile in the focal plane after being reflected. With the specifications in table 5.2 (page 29) the profile is imaged along the y-axis of the focal plane and *WIDTH* and *LENGTH* are oriented along the axes of the reference frame. This means that both parameters can be obtained by simply determining the RMS along the corresponding axis.
The resulting showers can be seen in fig 5.6.

Tab. 5.2.: Chosen parameters for a gaussian shower profile

Parameter	*Distribution*	*Typ1*	*Typ2*
x	uniform	$[-200, 200]$ cm	
y	uniform	$[-200, 200]$ cm	
production height	constant	10 km	
# photons	constant	100000	
tilt angle Θ_{tilt}	linear	$[0, 2]°$ in 41 steps	
u	normal	$\mu = 90° \quad \sigma = 0.2°$	$\mu = 90° \quad \sigma = 0.4°$
v	normal	$\mu = 90° - \alpha \quad \sigma = 0.4°$	$\mu = 90° - \alpha \quad \sigma = 0.2°$

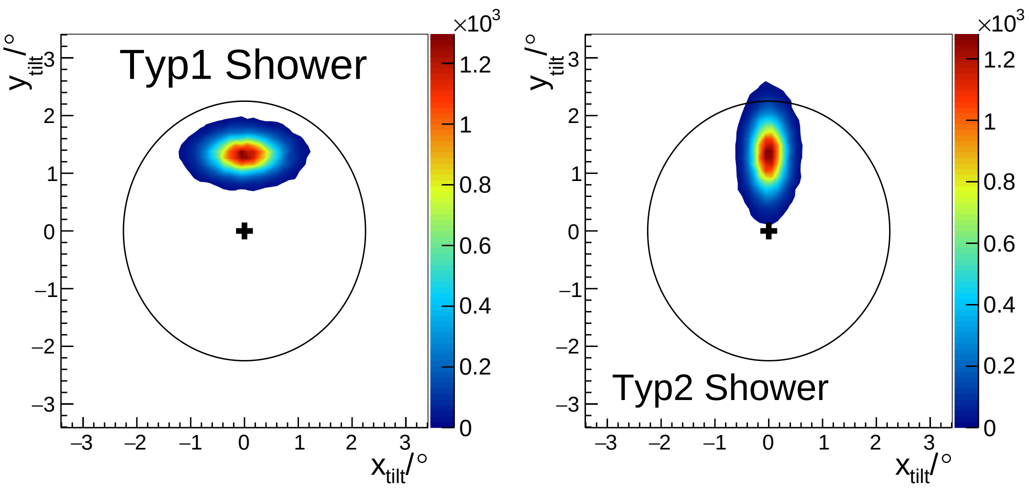

Fig. 5.6.: Shower profile in the focal plane after ray tracing. The black cross is positioned at the camera centre whereas the circle shows the size of the actual sensitive area.

5.3.1 Correction of the Hillas parameters

The ray tracing results are evaluated calculating the *DIST*, *LENGTH* and *WIDTH* for each photon distribution in the focal plane. The obtained values are plotted against the tilt angle Θ of the incident photons.
Once more, a straight line is fitted to reveal any changes in the quantities due to the image correction.

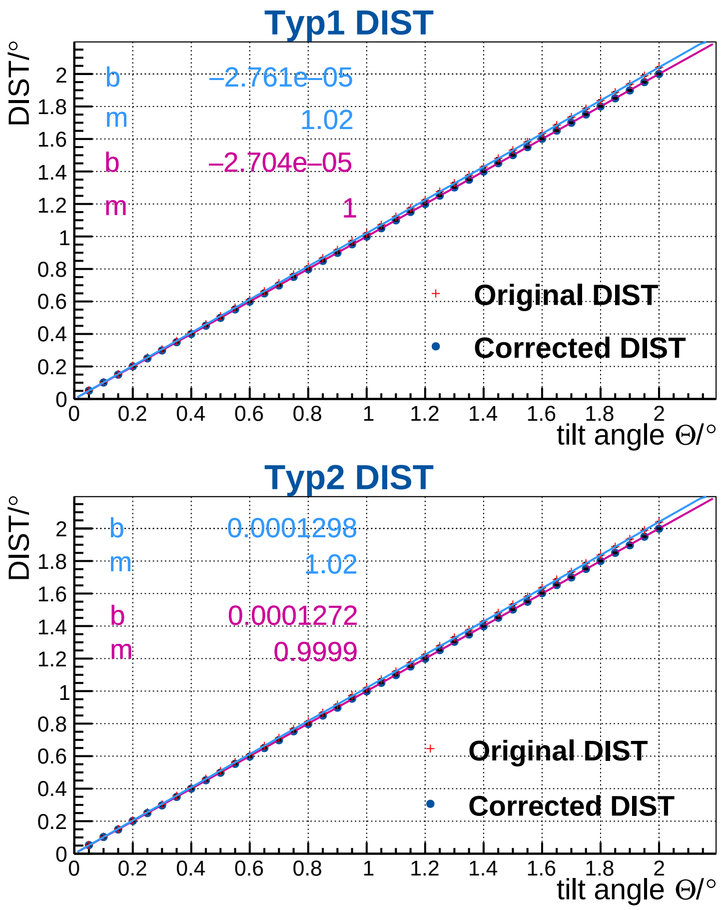

Fig. 5.7.: Correction of DIST. *Upper figure*: Typ1. *Lower figure*: Typ2

The chosen distributions are large in comparison to the point source images examined in the previous section. Therefore, the influence of the binning is not dominant here. As expected the DISTs are corrected by the maximum factor of $\eta = \frac{0.02°}{1°}$ for both shower types (fig. 5.7).
More interesting are the WIDTH and LENGTH. The corrected lengths differ from the originals by a constant of approximately

$$\Delta\text{LENGTH} = 0.008° \tag{5.3}$$

respectively (fig. 5.8). The WIDTHs differ by approximately

$$\Delta\text{WIDTH} = 0.004° \tag{5.4}$$

(fig. 5.9). Both constants can be explained multiplying the RMS by the correction factor η. For these extreme photon distribution WIDTH and LENGTH are also corrected by the maximum possible amount of 2%.

The result of the examination is now that the image parameters of shower-like photon distributions will be maximal corrected if the statistics and the size of the shower is large enough. This means, the principle of the image correction was successfully proved. Through the linear character, the image correction becomes especially valuable for showers that lie on the edge of the camera.

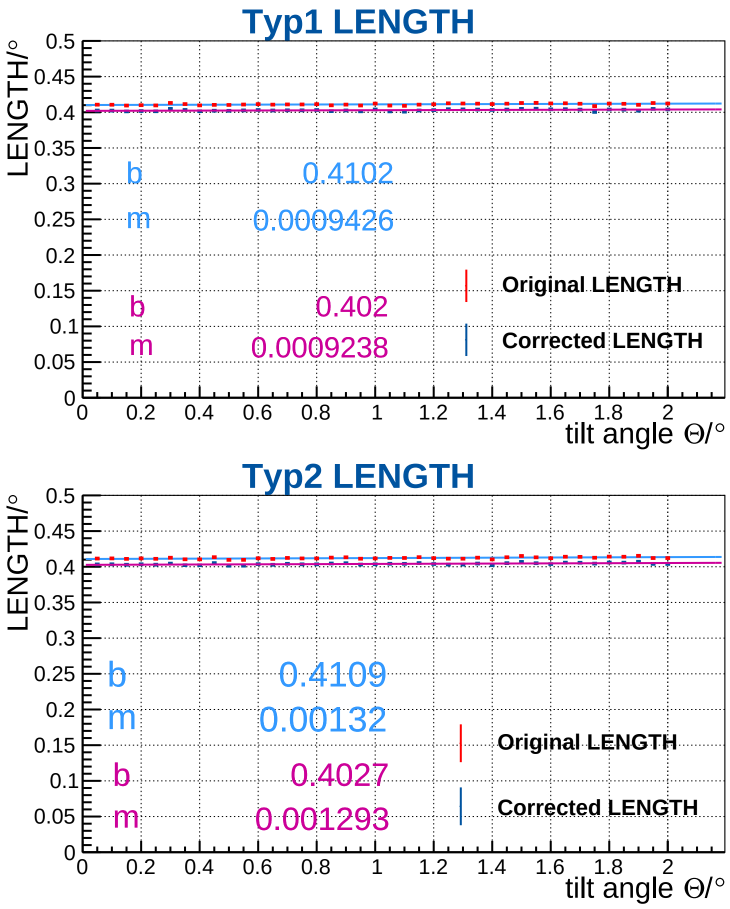

Fig. 5.8.: Correction of LENGTH. *Upper figure*: Typ1. *Lower figure*: Typ2

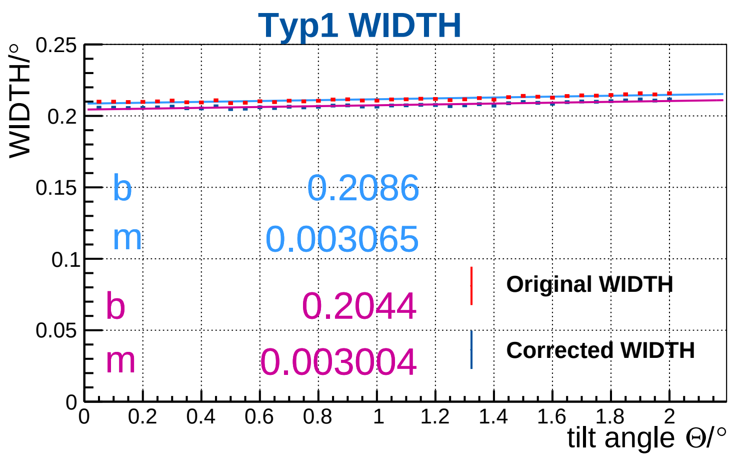

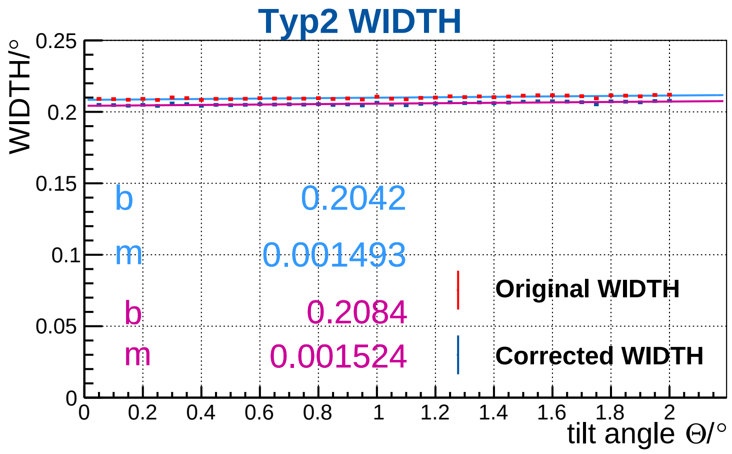

Fig. 5.9.: Correction of WIDTH. *Upper figure*: Typ1. *Lower figure*: Typ2

6 Conclusion and Outlook

A new image correction method for the First G-APD Cherenkov Telescope was introduced correcting the image in the camera by a maximum of 2% in the image parameters. The symmetry of the FACT reflector was proved observing a similar imaging quality than for the Davies Cotton reflector. The deviation from a perfect imaging system was determined to be a factor

$$\eta = \frac{0.02^\circ}{1^\circ}. \tag{6.1}$$

The impact of the binning was examined showing an oscillating behaviour for small photon distributions. Further, the image correction was applied on extreme examples of shower events proving that the image parameters can be corrected by the maximum 2% if enough statistics is provided. This is less than the 7% for the MAGIC I mirror which was expected because this mirror is parabolic and thus has a even larger deviation from the ideal image than the observed reflector in this thesis [31].

So far, having examined only idealised systems, it was not proved whether the image correction method contributes to an enhanced sensitivity of the telescope. This can only be determined using Monte Carlo simulations applying the method to realistic shower events. I would integrate the image correction method in the analysis step of the Hillas parameter determination. At this point, the impact on the parameter distributions could be worked out and the influence on the cut thresholds determined.

Before that, further investigations are needed concerning the other Hillas parameters such as the orientation angle α. Having elliptical shower images with an orientation which is not necessarily parallel to the axis of the camera reference frame, the image correction could change the corresponding orientation angle α causing an unintended rotation of the shower axis.

All together, the method offers a promising and above all simple way to contribute to the improvement of the sensitivity of the First G-APD Cherenkov Telescope.

Bibliography

[1] J. Hester NASA ESA and A. Loll. *A Giant Hubble Mosiac of the Crab Nebula*. URL: http://hubblesite.org/gallery/album/entire/pr2005037a/ (visited on June 22, 2016) (cit. on p. 1).

[2] T.C. Weekes. *Very High Energy Gamma-Ray Astronomy*. IOP Publishing Ltd, 2003 (cit. on pp. 1, 3, 4).

[3] J. Blümer, R. Engel, and J. R. Hörandel. „Cosmic rays from the knee to the highest energies“. In: *Progress in Particle and Nuclear Physics* 63 (Oct. 2009), pp. 293–338. arXiv: 0904.0725 [astro-ph.HE] (cit. on p. 2).

[4] K. Greisen. „End to the Cosmic-Ray Spectrum?“ In: *Phys. Rev. Lett.* 16 (1966) (cit. on p. 2).

[5] J. Jelley. *Cerenkov Radiation and its application*. Pergamon Press, 1958 (cit. on p. 3).

[6] I. Bekman. „Measurement of Cherenkov light with the HEAT telescope at the Pierre Auger Observatory“. Master's thesis. Germany: RWTH Aachen, July 2012 (cit. on p. 3).

[7] G. Mohanty. „The properties of Very High Energy gamma ray sources observed using the air Cherenkov technique“. In: *Retrospective Theses and Dissertations. Paper 11072* (1995) (cit. on pp. 4, 5).

[8] V.A. Acciari, T. Arlen, T. Aune, et al. „Observation of Markarian 421 in TeV gamma rays over a 14-year time span“. In: *Astroparticle Physics* 54 (2014), pp. 1 –10 (cit. on p. 4).

[9] A. M. Hillas, C. W. Akerlof, S. D. Biller, et al. „The Spectrum of TeV Gamma Rays from the Crab Nebula“. In: *The Astrophysical Journal* 503.2 (1998), p. 744 (cit. on p. 4).

[10] M Bustamante, G Carrillo Montoya, W de Paula, et al. „High-energy cosmic-ray acceleration“. In: (2010) (cit. on p. 4).

[11] J. Quinn, I. H. Bond, P. J. Boyle, et al. „The Flux Variability of Markarian 501 in Very High Energy Gamma Rays“. In: *The Astrophysical Journal* 518.2 (1999), p. 693 (cit. on p. 4).

[12] T. Bretz, M. Backes, D. Neise, et al. „Long Term VHE monitoring of bright blazars with a dedicated Cherenkov telescope“. In: *Workshop on Blazar Variability across the Electromagnetic Spectrum* (2008) (cit. on p. 4).

[13] M. De Naurois. „Analysis Methods for Atmospheric Cerenkov Telescopes“. In: (2005) (cit. on p. 6).

[14] A.M. Hillas. „Cerenkov light images of EAS produced by primary gamma“. In: *International Cosmic Ray Conference* 3 (Aug. 1985) (cit. on p. 6).

[15] H Anderhub, M Backes, A Biland, et al. „Design and operation of FACT – the first G-APD Cherenkov telescope“. In: *Journal of Instrumentation* 8.06 (2013), P06008 (cit. on pp. 9, 11).

[16] A Biland, T Bretz, J Buß, et al. „Calibration and performance of the photon sensor response of FACT — the first G-APD Cherenkov telescope“. In: *Journal of Instrumentation* 9.10 (2014), P10012 (cit. on pp. 10, 23).

[17] R. Winston, J.C. Minano, and P. Benitez. *Nonimaging Optics*. Elsevier Academic Press, 2005 (cit. on p. 10).

[18] I. Braun. „Solid light concentrator for Cherenkov Astronomy“. In: *Proceedings of the 31st ICRC, LODZ* (2009) (cit. on p. 10).

[19] A-K. Overkemping. „Justage der Spiegel und Simulation der realen Reflektorgeometrie für FACT“. Diplomarbeit. Germany: TU Dortmund, Mar. 2012 (cit. on pp. 11, 14–16).

[20] S. Müller. „Clear Sight in Cherenkov Astronomy Investigations on Reflector Geometry and Mirror Alignment for the FACT telescope“. Master’s thesis. Germany: TU Dortmund, 2014 (cit. on pp. 11, 12, 14).

[21] J.M. Davies and E.S. Cotton. „Design of the quartermaster solar furnace“. In: *Solar Energy* 1 (Apr. 1957), pp. 16–22 (cit. on p. 11).

[22] M. L. Ahnen and et al. „Bokeh Mirror Alignment for Cherenkov Telescopes“. In: *Astropart. Phys.* 82 (2016), pp. 1–9 (cit. on p. 11).

[23] M. L. Ahnen and et al. „Normalized and Asynchronous Mirror Alignment for Cherenkov Telescopes“. In: *Astropart. Phys.* 82 (206), pp. 56–65 (cit. on p. 11).

[24] Rene Brun and Fons Rademakers. „ROOT - An Object Oriented Data Analysis Framework“. In: *Nucl. Inst. & Meth. in Phys. Res. A 389 (1997) 81-86.* (1996) (cit. on p. 13).

[25] T. Bretz. „Standard Analysis for the MAGIC Telescope“. In: *Proceedings of the 29th ICRC, Pune, India* (2005) (cit. on p. 13).

[26] T. Bretz and D. Dorner. „MARS-The Cherenkov Observatory edition“. In: *American Institute of Physics Conference Series*. Ed. by F. A. Aharonian, W. Hofmann, and F. Rieger. Vol. 1085. American Institute of Physics Conference Series. Dec. 2008, pp. 664–667 (cit. on p. 13).

[27] A.-K. Overkemping and Julia Thaele. „MAGIC I - Datenauswertung mit MARS Eine kurze Beschreibung der Analyseschritte und ihrer Ergebnisse“. In: (Aug. 2011) (cit. on p. 13).

[28] T. Bretz and D. Dorner. „MARS - CheObs ed. – A flexible Software Framework for future Cherenkov Telescopes“. In: *Astroparticle, Particle and Space Physics, Detectors and Medical Physics Applications*. Ed. by C. Leroy, P.-G. Rancoita, M. Barone, et al. Apr. 2010, pp. 681–687 (cit. on p. 14).

[29] M.Born and E.Wolf. *Principles of Optics*. Pergamon Press, 1980 (cit. on p. 14).

[30] E.Hecht. *Optics*. Addison Wesley Longman Inc., 2002 (cit. on p. 14).

[31] „private comunication“. In: () (cit. on p. 33).

Tab. 6.1.: Abbreviations and their Meaning

Abbreviation	Meaning
AGN	Active Galaxy Nucleus
CALLITO	Calibrate Light Signals and Time Offsets
CERES	Camera Electronics and Reflector Simulation
CoG	Centre Of Gravity
DWARF	Dedicated Multiwavelength AGN Research Facility
EAS	Extensive Air Shower
FACT	First G-APD Cherenkov Telescope
FoV	Field of View
GANYMED	Gammas Are Now Your Most Exciting Discovery
G-APD	Geiger-mode Avalanche Photodiode
IACT	Imaging Atmospheric Cherenkov Telescope
MARS	MAGIC Analysis and Reconstruction Software
MARS CheObs ed.	Modular Analysis and Reconstruction Software - Cherenkov Observation Edition
NAMOD	Normalized and Asynchronous Mirror Orientation Determination
PDE	Photon Detection Efficiency
PMT	Photomultiplier Tube
PSF	Point Spread Function
RMS	Root Mean Square
SiPm	Silicon Photomultiplier
SNR	Supernova Remnant
SPONDE	Spectrum On Demand
STAR	Standard Analysis and Reconstruction
VHE	Very High-Energetic
VHEGR	Very High-Energetic Gamma Ray

A

Azimuthal distribution and Resource files

A.1 Distributions

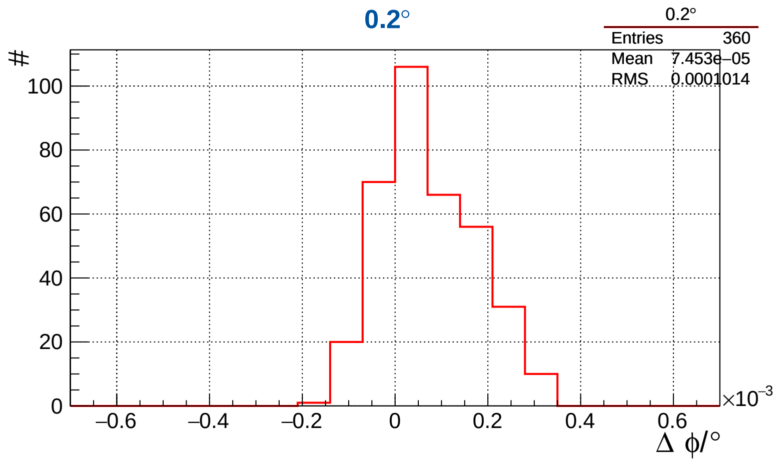

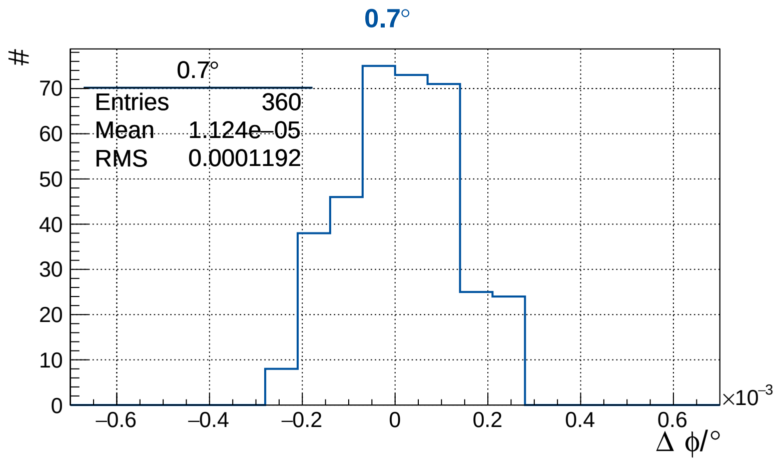

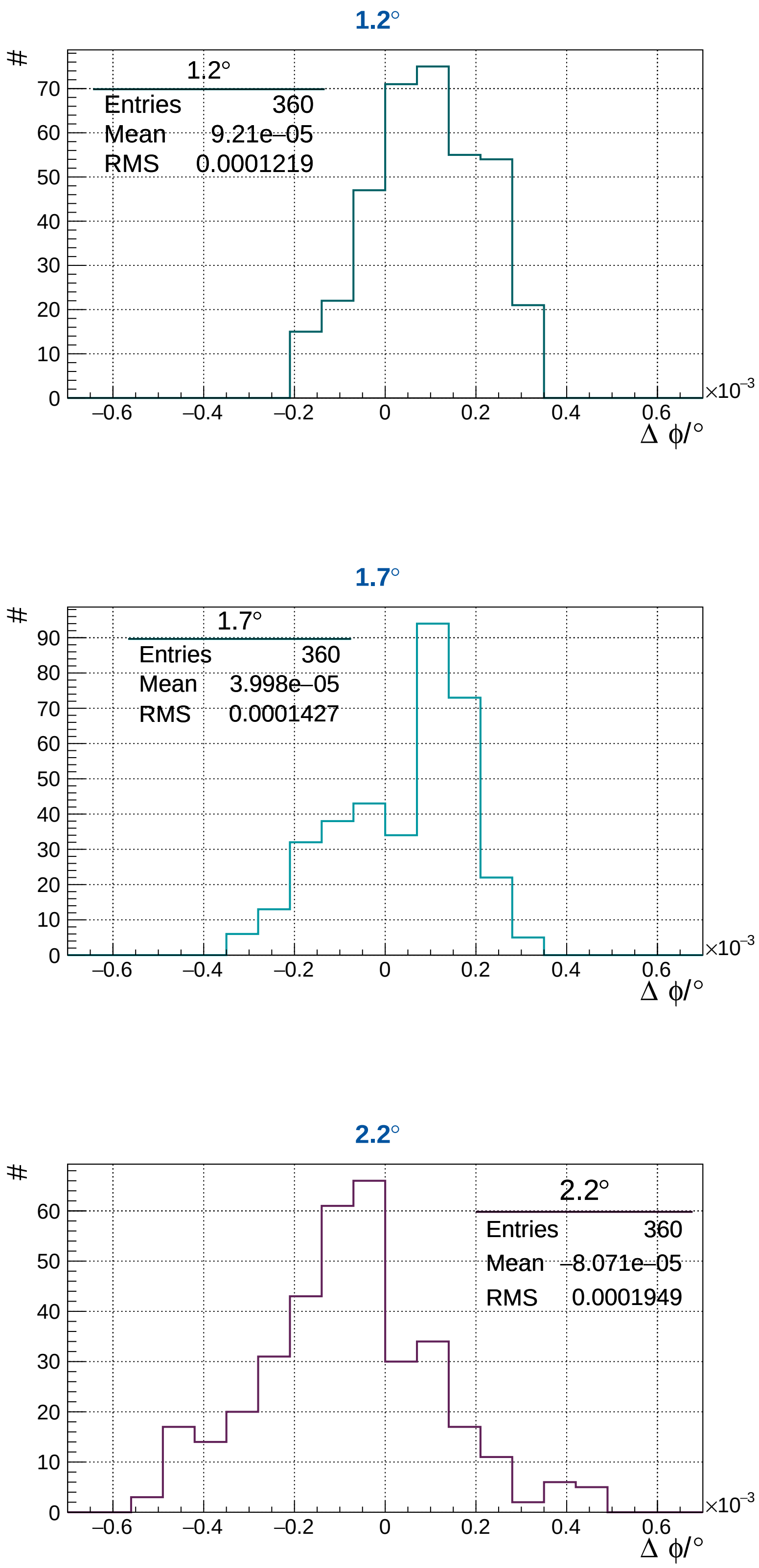

Fig. A.1.: In the figures above the distributions of the azimuthal deviation for the Davies Cotton reflector are presented. The mean of each figure lies only in the order of magnitude of $10^{-5} \cdot 1^\circ$ from zero away. The distributions are normal distributions.

A.2 FACT resource file

```
#ID 33
-31.68 -163.17 26.36 0.0324 0.1683 0.9852 490.2 Hex 60.6
#ID 21
30.73 -162.28 25.98 -0.0319 0.1676 0.9853 490.2 Hex 60.6
#ID 27
-125.17 -108.70 26.20 0.1291 0.1122 0.9853 489.4 Hex 60.6
#ID 3
-62.29 -108.20 16.62 0.0641 0.1115 0.9917 488.8 Hex 60.6
#ID 23
-0.48 -108.87 13.71 0.0003 0.1124 0.9937 488.4 Hex 60.6
#ID 6
61.71 -108.60 16.64 -0.0638 0.1122 0.9916 488.8 Hex 60.6
#ID 10
126.05 -109.54 26.64 -0.1301 0.1129 0.9851 489.4 Hex 60.6
#ID 34
-155.78 -54.55 25.94 0.1605 0.0562 0.9854 490.2 Hex 60.6
#ID 7
-93.59 -54.25 13.55 0.0967 0.0563 0.9937 488.5 Hex 60.6
#ID 30
-30.99 -54.25 7.34 0.0320 0.0558 0.9979 487.6 Hex 60.6
#ID 32
32.21 -54.10 7.40 -0.0337 0.0558 0.9979 488.1 Hex 60.6
#ID 2
94.03 -54.25 13.64 -0.0971 0.0558 0.9937 488.7 Hex 60.6
#ID 17
156.95 -55.04 26.40 -0.1616 0.0569 0.9852 490.0 Hex 60.6
#ID 5
-124.25 0.27 16.47 0.1281 0.0001 0.9918 488.9 Hex 60.6
#ID 12
-62.88 0.12 7.39 0.0650 0.0001 0.9979 488.4 Hex 60.6
#ID 26
63.47 0.20 7.47 -0.0656 -0.0005 0.9979 488.2 Hex 60.6
#ID 4
124.56 0.02 16.55 -0.1286 -0.0002 0.9917 489.1 Hex 60.6
#ID 18
-155.90 53.78 25.89 0.1607 -0.0558 0.9854 490.1 Hex 60.6
#ID 22
-93.20 54.20 13.47 0.0963 -0.0559 0.9938 488.5 Hex 60.6
#ID 16
-31.65 54.32 7.39 0.0326 -0.0562 0.9979 488.3 Hex 60.6
#ID 25
30.60 54.07 7.29 -0.0313 -0.0558 0.9980 488.2 Hex 60.6
#ID 24
93.71 54.62 13.62 -0.0966 -0.0565 0.9937 488.6 Hex 60.6
#ID 11
155.50 55.11 25.91 -0.1603 -0.0560 0.9855 490.0 Hex 60.6
#ID 31
-124.90 108.60 26.10 0.1289 -0.1119 0.9853 489.4 Hex 60.6
#ID 29
-62.27 107.90 16.55 0.0643 -0.1113 0.9917 488.8 Hex 60.6
#ID 35
-0.38 108.42 13.61 0.0006 -0.1120 0.9937 488.5 Hex 60.6
#ID 19
61.12 108.97 16.65 -0.0629 -0.1126 0.9916 489.0 Hex 60.6
```

A.3 FACT resource file

```
#ID 15
125.03 110.20 26.52 -0.1288 -0.1138 0.9851 489.5 Hex 60.6
#ID 13
-31.46 162.50 26.11 0.0325 -0.1678 0.9853 490.1 Hex 60.6
#ID 14
31.20 162.47 26.08 -0.0320 -0.1677 0.9853 490.0 Hex 60.6

# ID
# x[cm] y[cm] z[cm] Nx[1] Ny[1] Nz[1] f[cm] Type fD[cm]
#--------------------------------------------------------------------
----
#
# The FACT reflector right after reflector reconfiguration and
# alignment in May 2014.
#
# Mirror positions x and y are measured using an aperture photograph
of
# FACT.
#
# Mirror position z is measured using the remote controlled
# Laser Distance Meter. The distances from the mirror centers
towards
# the center of the focal plane are chosen to form a Hybrid
reflector
# half Davies Cotton half Paraboloid.
#
# The mirror orientation is measured using the advanced SCCAN system
# made for FACT's alignment. Here the orientations are expressed
using
# the normal vector of the mirror facets Nx, Ny and Nz.
#
# Focal length f is taken from Ann-Kristin Overkemping's Diploma
Thesis:
#           Justage der Spiegel und Simulation der realen
#                    Reflektorgeometrie fuer FACT
#
# The mirror diameter fD is taken to be equal for all mirrors and
has
# not been measured again.
#
# The ID is the number written on the back of the actual mirrors
mounted
# on FACT. It is the same ID numbering as used in Ann-Kristin
# Overkemping's Diploma Thesis.
#
# A detailed description of the calculations towards this numbers is
# found in Sebastian Mueller's Master Thesis, see appendix:
#                           Clear Sight
#                     in Cherenkov Astronomy
#              Investigations of Reflector Geometry
#                   and Mirror Alignment for the
#                         FACT Telescope
```

A.4 Davies Cotton resource file

```
#x[cm] y[cm] z[cm] Nx[1] Ny[1] Nz[1] f[cm] Type fD[cm]
62.00 0.00 12.90 -0.0647 0.0000 0.9979 490.2 Hex 60.6
31.00 53.69 12.90 -0.0324 -0.0560 0.9979 490.2 Hex 60.6
-31.00 53.69 12.90 0.0324 -0.0560 0.9979 489.4 Hex 60.6
-62.00 0.00 12.90 0.0647 0.0000 0.9979 488.8 Hex 60.6
-31.00 -53.69 12.90 0.0324 0.0560 0.9979 488.4 Hex 60.6
31.00 -53.69 12.90 -0.0324 0.0560 0.9979 488.8 Hex 60.6
92.66 53.50 20.81 -0.0971 -0.0561 0.9937 489.4 Hex 60.6
0.00 107.00 20.81 0.0000 -0.1121 0.9937 490.2 Hex 60.6
-92.66 53.50 20.81 0.0971 -0.0561 0.9937 488.5 Hex 60.6
-92.66 -53.50 20.81 0.0971 0.0561 0.9937 487.6 Hex 60.6
-0.00 -107.00 20.81 0.0000 0.1121 0.9937 488.1 Hex 60.6
92.66 -53.50 20.81 -0.0971 0.0561 0.9937 488.7 Hex 60.6
124.00 0.00 24.94 -0.1302 0.0000 0.9915 490.0 Hex 60.6
62.00 107.39 24.94 -0.0651 -0.1128 0.9915 488.9 Hex 60.6
-62.00 107.39 24.94 0.0651 -0.1128 0.9915 488.4 Hex 60.6
-124.00 0.00 24.94 0.1302 0.0000 0.9915 488.2 Hex 60.6
-62.00 -107.39 24.94 0.0651 0.1128 0.9915 489.1 Hex 60.6
62.00 -107.39 24.94 -0.0651 0.1128 0.9915 490.1 Hex 60.6
154.11 56.09 37.28 -0.1628 -0.0593 0.9849 488.5 Hex 60.6
125.63 105.42 37.28 -0.1327 -0.1114 0.9849 488.3 Hex 60.6
28.48 161.51 37.28 -0.0301 -0.1707 0.9849 488.2 Hex 60.6
-28.48 161.51 37.28 0.0301 -0.1707 0.9849 488.6 Hex 60.6
-125.63 105.42 37.28 0.1327 -0.1114 0.9849 490.0 Hex 60.6
-154.11 56.09 37.28 0.1628 -0.0593 0.9849 489.4 Hex 60.6
-154.11 -56.09 37.28 0.1628 0.0593 0.9849 488.8 Hex 60.6
-125.63 -105.42 37.28 0.1327 0.1114 0.9849 488.5 Hex 60.6
-28.48 -161.51 37.28 0.0301 0.1707 0.9849 489.0 Hex 60.6
28.48 -161.51 37.28 -0.0301 0.1707 0.9849 489.5 Hex 60.6
125.63 -105.42 37.28 -0.1327 0.1114 0.9849 490.1 Hex 60.6
154.11 -56.09 37.28 -0.1628 0.0593 0.9849 490.0 Hex 60.6

#/////////////////////////////////////////////////////
#* This file contains the setup for an ideal Davies-Cotton
reflector.
#* Since it is totally symmetric, an identification number was
#omitted.
#* The setup was calculated using the formulae from the
#* „Clear Sight in Cherenkov Astronomy - Investigations of Reflector
#Geometry and
#* Mirror Alignment for the FACT Telescope“ from Sebastian Müller.
#*/////////////////////////////////////////////////////
```